The Fornax3D project: planetary nebulae catalogue and independent distance measurements to Fornax cluster galaxies

Spriggs, T.W.; Sarzi, M.; Galán-de Anta, P.M.; Napiwotzki, R.; Viaene, S.; Nedelchev, B.; ... ; Zhu, L.

Astronomy & Astrophysics manuscript no. catalogue_paper
November 26, 2021

The Fornax3D project: Planetary nebulae catalogue and independent distance measurements to Fornax cluster galaxies⋆

T. W. Spriggs[1], M. Sarzi[2], P. M. Galán-de Anta[2,3], R. Napiwotzki[1], S. Viaene[4], B. Nedelchev[2], L. Coccato[5], E. M. Corsini[6,7], K. Fahrion[5], J. Falcón-Barroso[8,9], D. A. Gadotti[5], E. Iodice[10,5], M. Lyubenova[5], I. Martín-Navarro[11,8,9], R. M. McDermid[12,13], L. Morelli[18], F. Pinna[11], G. van de Ven[14], P. T. de Zeeuw[15,16], and L. Zhu[17]

[1] Centre for Astrophysics Research, University of Hertfordshire, College Lane, Hatfield AL10 9AB, UK
e-mail: tspriggs@outlook.com
[2] Armagh Observatory and Planetarium, College Hill, Armagh BT61 9DG, Northern Ireland, UK
[3] Astrophysics Research centre, School of Mathematics and Physics, Queen's University Belfast, Belfast BT7 INN, UK
[4] Sterrenkundig Observatorium, Universiteit Gent, Krijgslaan 281, 9000 Gent, Belgium
[5] European Southern Observatory, Karl-Schwarzschild-Straße 2, 85748 Garching bei Muenchen, Germany
[6] Dipartimento di Fisica e Astronomia 'G. Galilei', Università di Padova, vicolo dell'Osservatorio 3, 35122 Padova, Italy
[7] INAF–Osservatorio Astronomico di Padova, vicolo dell'Osservatorio 5, 35122 Padova, Italy
[8] Instituto de Astrofísica de Canarias, Calle Vía Láctea s/n, 38200 La Laguna, Tenerife, Spain
[9] Depto. Astrofísica, Universidad de La Laguna, Calle Astrofísico Francisco Sánchez s/n, 38206 La Laguna, Tenerife, Spain
[10] INAF–Osservatorio Astronomico di Capodimonte, Salita Moiariello 16, 80131, Naples, Italy
[11] Max-Planck-Institut für Astronomie, Königstuhl 17, 69117 Heidelberg, Germany
[12] Astronomy, Astrophysics and Astrophotonics Research Centre, Department of Physics and Astronomy, Macquarie University, Sydney, NSW 2109, Australia
[13] ARC Centre of Excellence for All Sky Astrophysics in 3 Dimensions (ASTRO 3D), Australia
[14] Department of Astrophysics, University of Vienna, Türkenschanzstraße 17, 1180 Vienna, Austria
[15] Sterrewacht Leiden, Leiden University, Postbus 9513, 2300 RA Leiden, The Netherlands
[16] Max-Planck-Institut für extraterrestrische Physik, Gießenbachstraße, 85741 Garching bei München, Germany
[17] Shanghai Astronomical Observatory, Chinese Academy of Sciences, 80 Nandan Road, Shanghai 200030, China
[18] Instituto de Astronomía y Ciencias Planetarias, Universidad de Atacama, Avenida Copayapu 485, Copiapó, Chile

Received ; accepted

ABSTRACT

Extragalactic planetary nebulae (PNe) offer a way to determine the distance to their host galaxies thanks to the nearly universal shape of the planetary nebulae luminosity function (PNLF). Accurate PNe distance measurements rely on obtaining well-sampled PNLFs and the number of observed PNe scales with the encompassed stellar mass. This means either disposing of wide-field observations or focusing on the bright central regions of galaxies. In this work we take this second approach and conduct a census of the PNe population in the central regions of galaxies in the Fornax cluster, using VLT/MUSE data for the early-type galaxies observed over the course of the Fornax3D survey. Using such integral-field spectroscopic observations to carefully separate the nebular emission from the stellar continuum, we isolated [O III] 5007 Å sources of interest, filtered out unresolved impostor sources or kinematic outliers, and present a catalogue of 1350 unique PNe sources across 21 early-type galaxies, which includes their positions, [O III] 5007 Å line magnitudes, and line-of-sight velocities. Using the PNe catalogued within each galaxy, we present independently derived distance estimates based on the fit to the entire observed PNLF observed while carefully accounting for the PNe detection incompleteness. With these individual measurements, we arrive at an average distance to the Fornax cluster itself of 19.86 ± 0.32 Mpc ($\mu_{\rm PNLF}$= 31.49 ± 0.04 mag). Our PNLF distance measurements agree well with previous distances based on surface brightness fluctuations, finding no significant systematic offsets between the two methods as otherwise reported in previous studies.

Key words. (ISM:) planetary nebulae: general – galaxies: clusters: individual: Fornax – galaxies: elliptical and lenticular, cD – galaxies: distances and redshift – techniques: imaging spectroscopy

1. Introduction

Extragalactic planetary nebulae (PNe) are detectable at great distances, via their strong [O III] 5007 Å emission, with surveys extending out as far as the Coma Cluster, ∼ 100 Mpc, where PNe were detected within the intracluster medium (Gerhard et al. 2005). Their ionised [O III] 5007 Å emission is unresolved at such distances, and when embedded within the bright stellar continuum of the galaxy only a careful modelling of the stellar continuum allows one to measure the PNe [O III] flux. This is why traditionally the study of extragalactic PNe is focused in the halo region of galaxies, where the stellar background is minimal. Previous studies have applied a range of observation techniques for the task of detecting extragalactic PNe: photometric observations using either 'on-off' band imaging or narrow-band filters of regions outside the galaxy central core (McMillan et al. 1993;

⋆ Tables A.1 to A.36 are only available at the CDS via anonymous ftp to ... or via ...

Feldmeier et al. 2007; Herrmann et al. 2008), while counter-dispersed slit-less spectroscopy was employed for the Planetary Nebulae Spectrograph (PN.S) instrument, used in Douglas et al. (2007) and Coccato et al. (2009), and later in the extended PN.S (ePN.S) in Pulsoni et al. (2018). However, these techniques fall short when exploring the central regions of galaxy, where spectroscopy is instead needed to uncover the presence of PNe amidst the stellar background and diffuse ionised-gas emission. Integral-field spectroscopy is ideal in this respect, in particular when using instruments such as MUSE (Multi Unit Spectroscopic Explorer Bacon et al. 2010) which, with its large field-of-view allows one to efficiently map the PNe populations of nearby galaxies (e.g. Kreckel et al. 2017)

An example of the growing spatial coverage that single observations can now achieve, across a single galaxy, would be M31. Thanks to its relatively close proximity, the PNe are detectable across the entire galaxy (Ciardullo et al. 1989a; Merrett et al. 2006; Pastorello et al. 2013; Jacoby et al. 2013; Martin et al. 2018; Bhattacharya et al. 2019a,b).

Over the past 32 years, one of the chief motivations for detecting extragalactic PNe has been to use them as tracer for the stellar kinematics in the faint outskirts of galaxies, where direct spectroscopic measurement are prohibitive. Indeed, numerous studies have shown how PNe can be used in this way to probe the structure of galaxy stellar halos and to measure their dark matter content(Romanowsky et al. 2003; Merrett et al. 2006; Douglas et al. 2007; Coccato et al. 2009; Kafle et al. 2018; Martin et al. 2018; Longobardi et al. 2018; Pulsoni et al. 2018; Bhattacharya et al. 2019a). At the same time, research has also shown that the distribution of PNe absolute magnitudes in [O III] 5007 Å, M_{5007}, appears to be nearly invariant between galaxies, with a noticeable cut-off at the bright end (Jacoby et al. 1989; Ciardullo et al. 1989a; Jacoby 1989; Ciardullo et al. 1989b). Notable discrepancies around the invariant nature of the PNLF arise when observing beyond 2 magnitudes from the cut-off, with evidence of dips appearing towards the faint end of the PNLF within the Large and Small Magellanic Clouds (LMC and SMC, respectively), as found by Jacoby & De Marco (2002) and Hernández-Martínez & Peña (2009). As such, a generalised analytical planetary nebulae luminosity function (PNLF) was first proposed by Ciardullo et al. (1989a), who used the PNe observed in M31 as Cepheid Variable distance estimates to calibrate the PNLF bright-end absolute magnitude [O III] 5007 Å, M^*_{5007} at a value of −4.48 mag.

More recently, a value of $M^*_{5007} = -4.53 \pm 0.06$ mag has been decided on for galaxies with stellar populations that are more metal rich than the LMC (Ciardullo 2012), with the stated census that M^*_{5007} does fade in smaller, more metal-poor galaxies.

In regards to extra-galactic distance determinations, the PNLF method has proven itself a reliable and unique tool, in particular given that PNe are expected to reside within all types of galaxies. Supernovae type Ia (SNIa) measurements are indeed serendipitous by nature, whereas using surface brightness fluctuations (SBF) and Cepheid variable stars is restricted mostly only to early- and late-type galaxies, respectively. Previous works found evidence of a systematic difference between distances derived from the PNLF and SBF (Ciardullo et al. 1993), although more recently both Kreckel et al. (2017) and Hartke et al. (2017) found that their PNe-based distances, to NGC628 and M49 respectively, are in good agreement with SBF measurements. As for the application of the PNLF method to the Fornax cluster, beyond our previous work (Spriggs et al. 2020, hereafter S20), there are recorded efforts using the aforementioned photometry and slit-less spectroscopy approaches (McMillan et al. 1993; Teodorescu et al. 2005; Feldmeier et al. 2007). Each one reporting good agreement to the respective distances measurements available to their dates. Now though, with more detailed SBF, SNIa, and other distance estimators, we see that the Fornax cluster may be further away than the initial estimates ranging between 16 Mpc and 19 Mpc.

Here, we continue the detection work of S20, and carry out a census of PNe populations within the central, middle and halo regions of the remaining early-type galaxies (ETGs) of the Fornax3D (F3D) survey (Sarzi et al. 2018). We introduce our PNLF modelling methodology, improving upon the method of S20. We then report independent distance estimates for each galaxy, and compare our findings with other results and techniques from the literature.

This paper is organised as follows. In Sect. 2, we introduce the F3D data set, along with reduction steps. Sect. 3 reviews the process of PNe detection, filtering, and cataloguing, as introduced in S20, then develops on these practises through the introduction of our PNLF modelling approach and how we tested the robustness and reliability of this method. The PNe catalogue is introduced in Sect. 4, detailing the contents, with notes on objects of unique interest. This is accompanied by the PNLF distances and how they stack up against distance measurements from other methods. We also briefly discuss the 3D structure of the Fornax cluster, as prescribed by our PNLF distances. Finally, we wrap up our findings and draw some future perspectives in Sect. 5

2. Data

Our work uses the MUSE data of the F3D survey, in the Wide Field Mode (WFM) so as to reach a spatial sampling of $0.2'' \times 0.2''$ across a $1' \times 1'$ field of view (FOV). The wavelength coverage that MUSE spans 4650–9300 Å, with a spectral sampling of 1.25 Å pixel^{-1}. The Fornax3D survey included multiple MUSE pointings (between two and three) to cover extended objects, and to ensure in particular that observations for ETGs reached down to the same limiting surface brightness of $\mu_B = 25$ mag arcsec^{-2}. The survey ensured that the central pointings would be observed under good seeing conditions (for a FWHM $\leq 0.8''$) precisely to enable a study of point sources such as PNe and globular clusters (e.g. Fahrion et al. 2019) as well as of galactic nuclei. In the outer regions the main interest was to characterise the properties of stellar population in the faint outskirts of galaxies, which is why these regions were observed under more lenient seeing conditions but over longer exposure times.

The MUSE data was reduced using the MUSE pipeline (Weilbacher et al. 2012, 2016), within the ESOREFLEX (Freudling et al. 2013) environment, as reported in Sarzi et al. (2018) and Iodice et al. (2019b). The reduction phase deals with key steps such as telluric correction, sky-subtraction and absolute flux calibration. All datacubes have been flux calibrated and this flux calibration has been further verified using HST images, as in Sarzi et al. (2018) and S20. The Fornax3D data taken from different pointings were aligned and presented as a single mosaic in Iodice et al. (2019b). For the purposes of detecting PNe it is important to account for the different image quality of these different observations, and therefore here we analyse separately the combined observations from each individual pointing.

2.1. Residual cube preparation

Our PNe detection method is based on residual data, that is, reduced MUSE spectra that have first been analysed by the Galaxy

IFU Spectroscopy Tool pipeline [1] (GIST, Bittner et al. 2019) and finalised by removing the stellar continuum. The GIST pipeline employs both pPXF (Cappellari & Emsellem 2004; Cappellari 2017) and PyGandALF (see GIST documentation): the first handles spaxel-by-spaxel modelling of the stellar continuum, using the full MILES stars library of templates (Vazdekis et al. 2012, 2016) while the second focuses on the nebular emissions. The results of the GIST pipeline efforts are then utilised to produce a residual data cube after subtracting the modelled stellar continuum, which therefore still contains the emission lines. We then later re-fit the residual cube for [O III] emission only, imposing a fixed line-width on the emission lines. This was found in S20 to produce a better map in [O III] 5007 Å emissions, which led to a greater number of PNe detected.

3. Methods

3.1. Compiling the PNe catalogue

In order to detect and characterise PNe in our sample galaxies using the MUSE data we adopt the methodology that is described in full in S20[2] and which consists of the following steps:

Firstly, we carry out a spaxel-by-spaxel fit to the [O III] 4959,5007 Å emission line doublet in the residual cube, imposing a fixed intrinsic line-width of 30 km s^{-1} typical of unresolved PNe in order to better highlight the presence of such unresolved [O III] sources. Previously identified regions with diffuse nebular emission or with significant and systematic stellar-continuum fit residuals are masked.

Secondly, we extract MUSE residual minicubes around each candidate PNe source 1.8″×1.8″wide and over a 100 Å wavelength range. This is followed by the evaluation of the imaging point-spread function (PSF). This is achieved through the simultaneous fit of the residual minicubes for the four best-detected PNe candidate sources, in terms of their central value for the A/rN ratio, using the 3D cube-fitting process described in S20.

Thirdly, we fit for the PNe candidate total [O III] flux and kinematics using the 3D cube-fitting process of S20 while now holding the spatial distribution of the [O III] flux to that of the previously derived PSF. following this, we conduct an evaluation of the minicube fit quality and point-source detection. Candidate PNe with central A/rN ratio less than three are deemed undetected and are discarded, as are sources whose minicube fits returned χ^2 values above the 3σ limit for the χ^2 statistics (for the given number of degree of freedom).

Finally, we conduct a spectral characterisation and PNe impostor identification process. After extracting PSF-weighted aperture spectra around each PNe candidate sources (from the original MUSE cube) we used GIST's GandALF fits along to extract Hβ, Hα, [N II] 6583 and [S II] 6716,6731 doublet line measurements, subsequently identifying PNe impostor sources from supernovae remnants or compact H II regions using diagnostic diagrams as seen in S20. This is accompanied by the identification of any kinematic interlopers among the remaining PNe candidate. PNe sources with exceedingly high or low velocities (beyond a 3 σ limit) compared to the stellar line-of-sight velocity distribution (LOSVD) along the PNe direction are not considered to belong to the galaxy under consideration.

Following these steps, we finally arrive at a catalogue of 1350 unique PNe across 21 ETGs in the Fornax cluster, located either within the central, middle or halo pointings of the F3D survey. For these objects, we list their spatial coordinates, line-of-sight velocities, as well as their measured fluxes, and magnitudes with appropriate errors, in the measured [O III] 5007Å emission lines. The catalogue also includes PNe impostor sources and PNe interlopers, as well as a handful of PNe objects that were considered to be over-luminous (see, e.g. the case of FCC 167 in S20) and which will also be excluded by our following PNLF analysis.

3.2. PNLF fitting and distance estimation

In S20 we followed the simplest approach for estimating the distance to a galaxy based on the brightest observed PNe. In this case the PNLF distance modulus is simply $\mu_{\rm PNLF} = {\rm m}_{5007,\rm min} - {\rm M}^*_{5007}$ where $\rm m_{5007,min}$ is the [O III] 5007 Å magnitude of the brightest PN and $\rm M^*_{5007}$ is the M31 Cepheid distance calibrated absolute magnitude of the PNLF bright cut off. This approach is relatively sound in the case of galaxies presenting a significant number of PNe (as in FCC 167 and FCC 219, the objects studied in S20) but will clearly lead to biased results when dealing with few PNe. Indeed in this case we are more likely to miss the rarest objects at the bright cut-off of the PNLF, thus deducing an overestimated distance.

Due to a large range in the number of PNe observed across our 21 galaxies, we decided to implement a distance estimation technique based on the entire observed PNLF, taking full advantage of our knowledge for the PNe-detection completeness function in each object in order to exploit the whole range of observed $\rm m_{5007}$ values. We follow the completeness correcting method of S20, assessing the level of incompleteness of our samples over the observed FOV. In short though, we calculate the completeness of detection for a given apparent magnitude (m_{5007}) from the fraction of galaxy stellar light within the MUSE FOV, where a PNe of that particular magnitude can be detected. This procedure is also informed by the PSF of the observation, along with the signal to noise cut of 3 × A/rN. This is also the method applied, and described, within Galán-de Anta et al. (2021).

Then, for each galaxy we explore the parameter space of $\mu_{\rm PNLF}$, evaluating for a value that would lead to a completeness-corrected PNLF model through simply minimising the Kolmogorov-Smirnov statistic D. To achieve this, we utilise the Python based Scipy package's 'KS_1samp' function, passing the supremum value (D) to the scalar minimiser of LMfit (Newville et al. 2014, 2019), applying the Nelder-Mead optimisation method (Nelder & Mead 1965). In terms of model PNLF, we used the analytic form provided by Longobardi et al. (2013)

$$N(M) = c_1\, e^{\,c_2\, M_{5007}}\, [1 - e^{\,3(M^*_{5007} - M_{5007})}], \quad (1)$$

where c_1 is a normalisation factor, c_2 defines the functional form of the PNLF, $\rm M^*_{5007}$ is the bright-end cutoff value first and finally, $\rm M_{5007}$ is the absolute magnitude of the PNe in [O III] 5007Å. In that follows we adopt the most recently calibrated values of $\rm M^*_{5007} = -4.53 \pm 0.06$ for the bright-end cut-off (Ciardullo 2012) and hold c_2 to the standard value of 0.307 derived by Ciardullo et al. (1989a). We note that systematic variations in $\rm M^*_{5007}$ have been reported at very low stellar metallicities, below [M/H] < -0.5 (Bhattacharya et al. 2021), but since only one of our objects (FCC 119, see Tab. 1C in Iodice et al. (2019a)) would appear to fall in this regime, such potential systematic effect would not greatly impact our overall results. Appendix A shows that in principle our methodology can estimate the c_2 parameter but also

[1] https://abittner.gitlab.io/thegistpipeline

[2] Code hosted on Github: https://github.com/tspriggs (Spriggs & gdapablo 2021)

that our current data do not provide strong evidence for departing from the assumed $c_2 = 0.307$ value. Since the KS-statistics is independent of normalisation, we effectively ignore c_1 while looking for the best $\mu_{\rm PNLF}$ value through our KS-statistic minimisation. Instead, we finally adjust the normalisation of our best completeness-corrected model for the observed PNLF by simply integrating it and matching the result to observed number of PNe. In this case, availing of the entire PNe sample allowsfor tighter constraints on any estimates for the total number of expected PNe by integrating the PNLF down to some magnitude limit, as this depends on the original Poisson uncertainty on the actual number of PNe used to constrain the PNLF model in first place.

To evaluate our uncertainties around our best $\mu_{\rm PNLF}$ values we resort to simulations. Namely, starting from the best-model PNLF (at the best $\mu_{\rm PNLF}$ and accounting for the completeness), we sample such a parent distribution N times to produce a N synthetic observed PNLF, which we then re-fit through our KS-statistic minimisation routine to obtain N best $\mu_{\rm PNLF}$ values. The $16^{\rm th}$ and $84^{\rm th}$ percentile of such a $\mu_{\rm PNLF}$ distribution provides our $\pm1\sigma$ uncertainties on the measured $\mu_{\rm PNLF}$. Typically, $N = 100$ deliver stable results. In sampling the best-model PNLF we account for Poisson statistics. For this, each time we sample the parent PNLF model we use a varying number drawn from a Poisson distribution with expectation value equal to the observed number of PNe. Accounting for Poisson statistics is necessary considering how the formation of PNe is itself a stochastic process. Put it simply, the observed number of PNe is likely to be different even if we were hypothetically to observe in the same way two identical galaxies at the same distance, which in turn would lead to slightly different PNLF distance estimates. To further account for observational errors in our magnitude measurements, we perturb our original data according to our measured errors and add in quadrature to the error budget the standard deviation for the $\mu_{\rm PNLF}$ distribution that is obtained in this way. Both accounting for Poisson statistics and observational errors contribute very little to the error budget, around 3% an 2%, respectively. Indeed, as will be shown in the next section, how well $\mu_{\rm PNLF}$ can be estimated depends primarily on the number of PNe and on depth of our detection completeness. Finally, we note that Ciardullo (2012) report a formal error of 0.06 mag for M^*_{5007}, which we also add in quadrature to our PNLF errors.

3.3. PNLF simulations

Simulations act as a useful diagnostic tool to understand how our PNLF modelling handles different PNe samples sizes ($N_{\rm PNe\,sim}$), especially when dealing with small PNe numbers where we wish to understand whether and to which extent our solution may be biased. The simulations are based on a finely sampled intrinsic PNLF model that assumes the standard $c_{2\,\rm in} = 0.307$ value, which is then shifted taking a distance modulus of $\mu_{\rm PNLF\,in} = 31.45$ mag and finally corrected for incompleteness. From such a parent PNLF profile we then draw $N_{\rm PNe\,sim}$ apparent $m_{5007\,\rm sim}$ values to create a large set of synthetic PNLF, with $m_{5007\,\rm sim}$ varying between 5 and 200 in order to cover the range of recorded $N_{\rm PNe}$ seen in our central pointings (Table 1). Each synthetic PNLF is then passed to our PNLF-fitting algorithm for parameter estimation.

Assuming the PNLF given in Eq. 1 and while only fitting for $\mu_{\rm PNLF}$, Fig. 1 shows how this parameter is recovered with increasing precision with increasing PNe sample size, without incurring in any significant bias even at low $N_{\rm PNe\,sim}$ numbers. The top panel of Fig. 1 is based on simulations that adopt the completeness profile observed in FCC 193, where our data allow one to detect PNe some 2.5 magnitudes below the PNLF bright cutoff, whereas the lower panel shows the case of FCC 147 where only probe the PNLF 1.5 magnitudes below this limit. In both instances the scatter in the recovered $\mu_{\rm PNLF}$ scales as $1/\sqrt{N_{\rm PNe\,sim}}$, but at a given number of PNe the accuracy in recovering $\mu_{\rm PNLF}$ would actually decrease for deeper the observations. Accounting within our simulation for the entire range of completeness functions observed across our sample (Fig. 2) produces an average trend with $N_{\rm PNe\,sim}$ for the scatter in the recovered $\mu_{\rm PNLF}$ that captures well the errors in our actual $\mu_{\rm PNLF}$ measurements for our 21 objects (Fig. 3). Overall, this exercise gives us confidence in our $\mu_{\rm PNLF}$ estimates and errors, even in objects with less than 20 PNe.

4. Results and discussion

In this section, we first review the catalogue of the PNe found within the ETG population of the F3D survey. Then, moving onto the results of applying our PNLF fitting method (see Sect. 3) to each galaxy. We then discuss the accuracy of the PNLF as a distance indicator, when compared to SBF measurements.

4.1. The F3D PNe catalogue

We present a catalogue of PNe detected across 21 galaxies, reporting a total of 1350 unique PNe. Though the PNe of each galaxy are our main interest, each galaxy's catalogue contains sources highlighted as impostors, following the criteria of S20. Such impostors are labelled, as described in Section 3.1, following the criteria of S20: supernova remnants (SNR), HII regions, and over-luminous sources (of which we find two in total; one each in FCC 167 and FCC 276). Only the sources in our catalogues that have the ID of 'PN' are used for the PNLF modelling and distance estimate efforts.

A sample of our catalogued PNe, from FCC 083, can be found in appendix A, where the two regions covered in the F3D survey are labelled as: 'center' and 'halo'. The rest of the catalogue is stored as digital records, uploaded to the VizieR On-line Data Catalog. The table contains a 'Source ID' column that follows the same naming convention introduced in S20, using the F3D label used at the start. The RA and Dec are included for future source cross-matching. 'm_{5007}' is the apparent magnitude of the [O III] 5007 Å emission. 'A/rN' is the amplitude-to-residual noise ratio, essentially a signal-to-noise measure. 'LOSV (km s^{-1})' is the reported observed line-of-sight velocity of the source, derived from the wavelength position of the [O III] 5007 Å emission line. The 'label' column states each source's assigned identity: PN, SNR (supernova remnant), HII (compact HII region), or OvLu (over luminous source). Finally, an index column is included for easier source comparison, highlighting sources that appear in the overlap of pointings: center C-00, middle M-00 and halo H-00.

All the galaxies in Table 1, are shown in Figs. C.2 and C.1. Every galaxy's FOV is shown via their signal-to-noise map in [O III] 5007 Å, with catalogued PNe circled. Alongside the FOV, we present the modelled PNLF of the catalogued sources. If there is halo or middle data present, they are also presented in different colours, as explained in the legends of each plot. The blue histograms show the distribution of detected PNe m_{5007} values, while the black line indicates a scaled form of the Jacoby (1989) form of the PNLF. We then scale this PNLF to

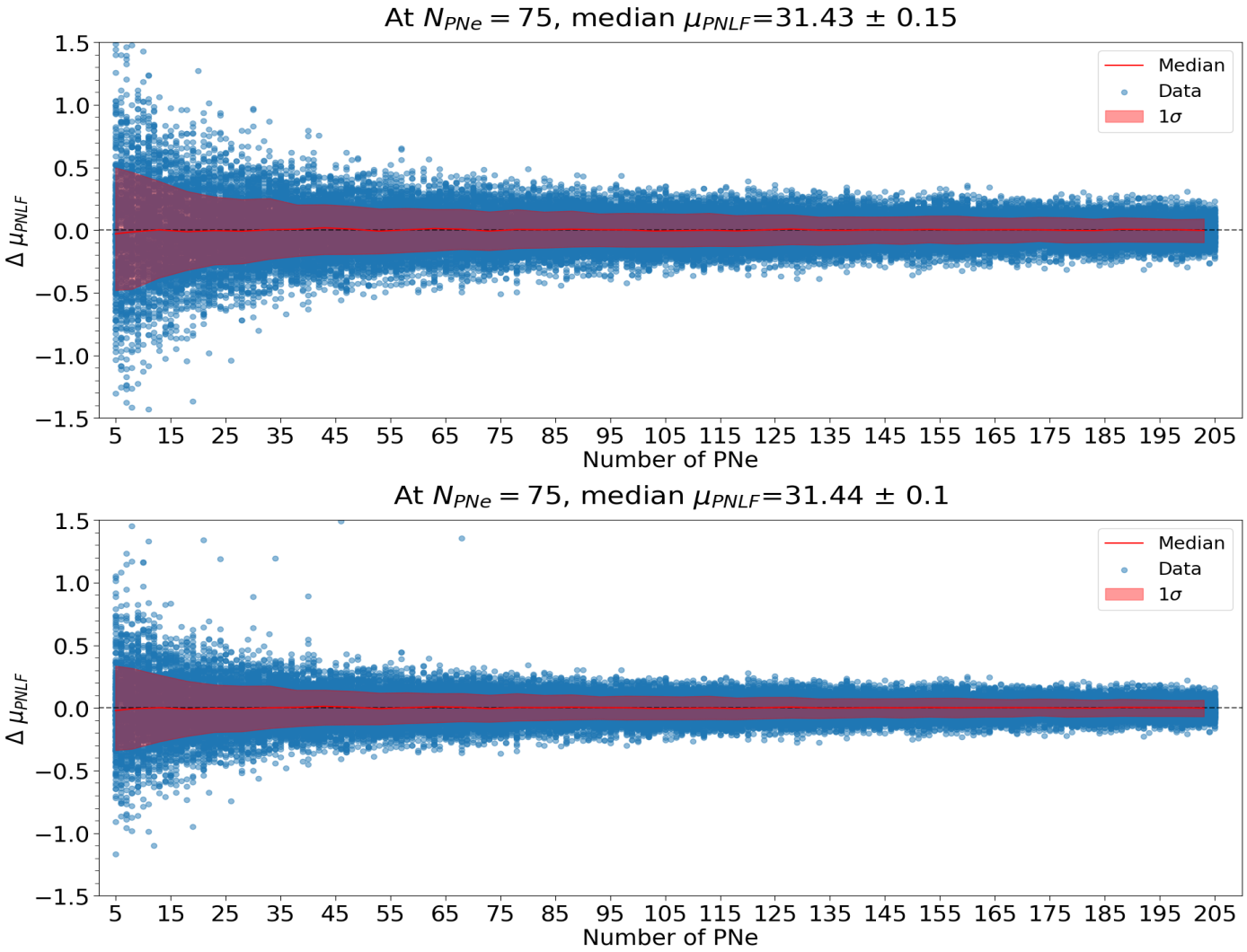

Fig. 1: Results of our simulations assessing the accuracy of our PNLF modelling, while holding to the standard form of the PNLF with a fixed $c_2 = 0.307$ value and optimising the distance modulus $\mu_{\rm PNLF}$. Each blue dot shows the difference $\Delta\mu_{\rm PNLF} = \mu_{\rm PNLF\,best-fit} - \mu_{\rm PNLF\,in}$ between the returned best-fit $\mu_{\rm PNLF}$ value and the input value when fitting synthetic PNLFs drawn from a parent incompleteness-corrected PNLF model with a varying $N_{\rm PNe\,sim}$ number of PNe. In this case, the parent distribution assumes a distance modulus $\mu_{\rm PNLF\,in} = 31.45$ and the same completeness function as observed in FCC 193 (top panel) and FCC 147 (bottom panel), which reaches about 2.5 and 1.5 magnitude below the apparent magnitude of the PNLF cutoff, respectively (see FCC147 FCC193 PNLF in Fig C.2). As $N_{\rm PNe\,sim}$ increases, the scatter in the $\Delta\mu_{\rm PNLF}$ values decreases while overall returning an unbiased answer, even at low $N_{\rm PNe\,sim}$, as traced also by the binned median red line. The red shaded region traces the 1σ confidence limit.

form the incompleteness-corrected PNLF, shown by dashed lines (colour dependant on pointing location). The blue shaded regions surrounding the C89 PNLF line, as well as the dashed incompleteness-corrected profile, show the 1 σ confidence limit. After reviewing the literature for works that may contain matching PNe, the only other surveys that contained such matches (for FCC 167 and FCC219 by Feldmeier et al. (2007) and McMillan et al. (1993) respectively) have already been discussed and compared with our samples in S20. We are then confident that we are cataloguing sources never before detected.

4.2. Dynamical tracers

The PNe observed within the central regions of a galaxy can be assumed to be travelling with the same systemic velocity of the galaxy. To this end, we can verify this assumption by taking the median of the LOSV values, as measured from the 3D fitting code, using the mean wavelength position to measure each PNe's individual LOSV. Fig. 4 shows the comparison of our median LOSV values, to those given by Iodice et al. (2019a), who present the heliocentric systemic velocity of each galaxy, as measured from the stars in the central regions. In agreement with our original assumption, we see that the PNe median LOSV values and Iodice et al. (2019a) systemic velocities are in very good agreement.

4.3. PNLF distances

Our deep MUSE data allow one to evaluate the accuracy and reliability of the standard candle nature of the PNLF, as an independent distance measurement technique. Using the PNe catalogue that we have produced we can now derive independent PNLF distance estimates for each of the 21 ETGs targeted by the F3D project as well as an overall average distance to the For-

Table 1: PNe numbers and distances to each ETG.

Galaxy	Pointing	$N_{\rm PNe}$	$N_{2.5}$	$\mu_{\rm PNLF}$ (mag)	$D_{\rm PNLF}$ (Mpc)	$\mu_{\rm SBF}$ (mag)	$\mu_{\rm CF2}$ (mag)	Alt. Name
(1)	(2)	(3)	(4)	(5)	(6)	(7)	(8)	(9)
FCC083	center	62	150^{+22}_{-19}	$31.34^{+0.14}_{-0.15}$	$18.53^{+1.23}_{-1.30}$	31.42 ± 0.07	31.42 ± 0.24	NGC 1351
FCC083	halo	19	26^{+7}_{-6}	–	–	–	–	–
FCC119	center	14	23^{+8}_{-6}	$31.71^{+0.40}_{-0.42}$	$21.97^{+4.10}_{-4.27}$	31.54 ± 0.10	31.52 ± 0.24	–
FCC143	center	13	45^{+16}_{-12}	$31.91^{+0.28}_{-0.27}$	$24.11^{+3.14}_{-2.95}$	31.43 ± 0.09	31.22 ± 0.24	NGC 1373
FCC147	center	98	270^{+30}_{-27}	$31.43^{+0.11}_{-0.11}$	$19.36^{+1.02}_{-0.99}$	31.46 ± 0.07	31.56 ± 0.24	NGC 1374
FCC147	halo	13	14^{+5}_{-4}	–	–	–	–	–
FCC148	center	57	128^{+19}_{-17}	$31.56^{+0.17}_{-0.16}$	$20.54^{+1.60}_{-1.55}$	31.50 ± 0.07	31.48 ± 0.14	NGC 1375
FCC148	halo	16	23^{+7}_{-6}	–	–	–	–	–
FCC153	center	44	128^{+22}_{-19}	$31.68^{+0.14}_{-0.17}$	$21.73^{+1.44}_{-1.66}$	31.59 ± 0.07	31.32 ± 0.24	IC 1963
FCC153	halo	41	75^{+14}_{-12}	–	–	–	–	–
FCC161	center	106	214^{+23}_{-21}	$31.47^{+0.13}_{-0.13}$	$19.67^{+1.19}_{-1.20}$	–	31.24 ± 0.24	NGC 1379
FCC161	halo	26	31^{+7}_{-6}	–	–	–	–	–
FCC167	center	108	402^{+43}_{-39}	$31.30^{+0.09}_{-0.10}$	$18.23^{+0.79}_{-0.87}$	31.57 ± 0.07	31.35 ± 0.15	NGC 1380
FCC167	middle	28	82^{+19}_{-15}	–	–	–	–	–
FCC167	halo	6	10^{+6}_{-4}	–	–	–	–	–
FCC170	center	41	133^{+24}_{-21}	$31.46^{+0.16}_{-0.15}$	$19.57^{+1.45}_{-1.38}$	31.70 ± 0.08	31.69 ± 0.28	NGC 1381
FCC170	halo	39	94^{+18}_{-15}	–	–	–	–	–
FCC177	center	55	72^{+11}_{-10}	$31.25^{+0.23}_{-0.24}$	$17.80^{+1.88}_{-1.95}$	31.51 ± 0.07	31.49 ± 0.28	NGC 1380A
FCC177	halo	19	24^{+7}_{-6}	–	–	–	–	–
FCC182	center	10	14^{+6}_{-4}	$31.20^{+0.48}_{-0.53}$	$17.35^{+3.84}_{-4.21}$	31.46 ± 0.09	31.44 ± 0.28	–
FCC184	center	69	268^{+36}_{-32}	$31.63^{+0.13}_{-0.13}$	$21.22^{+1.29}_{-1.23}$	31.43 ± 0.09	31.41 ± 0.28	NGC 1387
FCC184	middle	20	27^{+8}_{-6}	–	–	–	–	–
FCC184	halo	2	3^{+4}_{-2}	–	–	–	–	–
FCC190	center	25	54^{+13}_{-11}	$31.64^{+0.23}_{-0.26}$	$21.29^{+2.30}_{-2.54}$	31.54 ± 0.07	31.52 ± 0.28	NGC 1380B
FCC190	halo	8	22^{+11}_{-8}	–	–	–	–	–
FCC193	center	156	289^{+25}_{-23}	$31.46^{+0.12}_{-0.13}$	$19.59^{+1.10}_{-1.15}$	31.63 ± 0.07	31.42 ± 0.22	NGC 1389
FCC193	halo	19	23^{+7}_{-5}	–	–	–	–	–
FCC219	center	70	238^{+32}_{-28}	$31.47^{+0.11}_{-0.12}$	$19.71^{+1.04}_{-1.08}$	31.54 ± 0.07	31.37 ± 0.22	NGC 1404
FCC219	halo	16	18^{+6}_{-4}	–	–	–	–	–
FCC249	center	14	31^{+11}_{-8}	$31.41^{+0.30}_{-0.33}$	$19.17^{+2.62}_{-2.91}$	31.80 ± 0.08	31.82 ± 0.24	NGC 1419
FCC255	center	36	58^{+11}_{-10}	$31.42^{+0.24}_{-0.25}$	$19.20^{+2.10}_{-2.18}$	31.50 ± 0.07	31.48 ± 0.28	ESO 358-G050
FCC276	center	71	235^{+31}_{-28}	$31.48^{+0.12}_{-0.13}$	$19.76^{+1.13}_{-1.21}$	31.46 ± 0.07	31.50 ± 0.22	NGC 1427
FCC277	center	23	109^{+28}_{-23}	$31.88^{+0.19}_{-0.19}$	$23.76^{+2.07}_{-2.05}$	31.58 ± 0.08	31.56 ± 0.28	NGC 1428
FCC301	center	19	46^{+13}_{-10}	$31.64^{+0.27}_{-0.26}$	$21.24^{+2.60}_{-2.59}$	31.47 ± 0.08	31.06 ± 0.24	ESO 358-G059
FCC310	center	39	72^{+14}_{-12}	$31.53^{+0.24}_{-0.22}$	$20.21^{+2.27}_{-2.05}$	31.50 ± 0.07	31.48 ± 0.28	NGC 1460
FCC310	halo	50	68^{+11}_{-10}	–	–	–	–	–

Notes. Galaxies covered in this PNe catalogue, including entries for central, middle, and halo regions where covered. Galaxy name (1) and location (2), number of detected PNe (3), expected number of PNe (from PNLF) within 2.5 magnitudes of the bright-end cut-off (4), PNLF derived distance modulus (5) and corresponding distance in Mpc (6). We also include the latest distance modulus values of Blakeslee et al. (2009, 2010) (7) and from the CosmicFlows-3 catalogue (Tully et al. 2016) (8). Finally, the alternative galaxy name is provided for simpler identification (9).

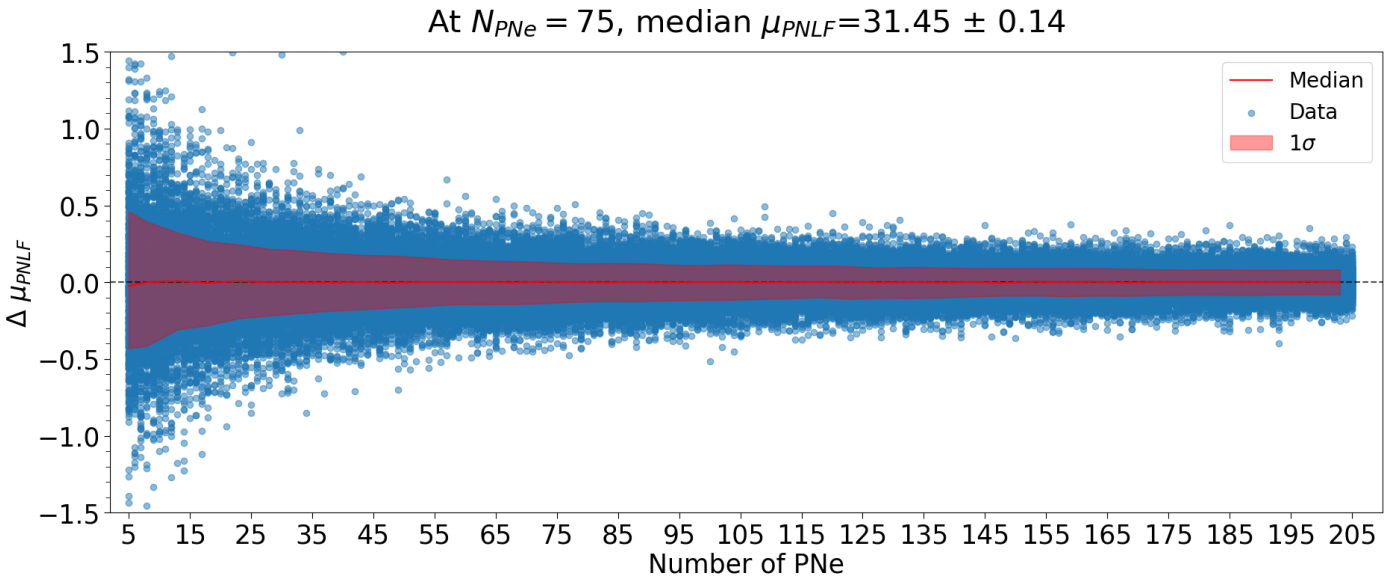

Fig. 2: Same as in Fig. 1, but now accounting in the simulations for the whole range of different completeness profiles observed across our sample.

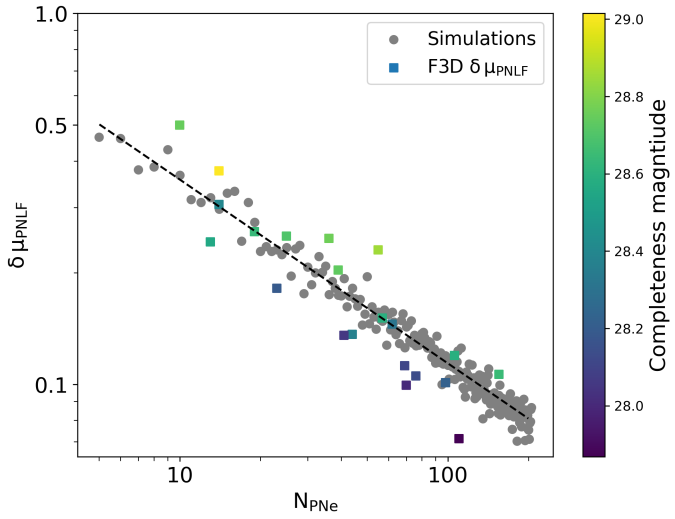

Fig. 3: Comparison between the average scatter in the recovered distance magnitude values from our simulations when accounting for the entire range of completeness profiles observed across our sample (grey circles) and the errors on the individual distance magnitude measurements in our sample galaxies (squares, colour-coded by completeness magnitude).

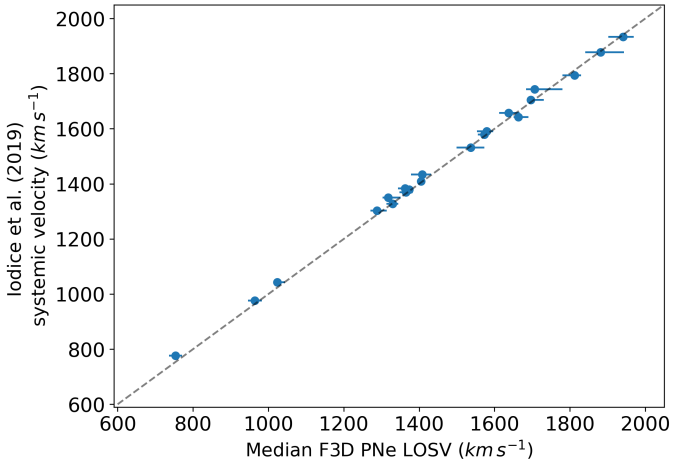

Fig. 4: Comparison between the systemic velocities of our sample galaxies as measured by Iodice et al. (2019a) from the stellar kinematic maps and as derived from the median PNe LOSV observed in the MUSE central pointing. The diagonal blue line indicates the one to one relation. Small residual offset may reflect an asymmetric sampling of the PNe around the centre of the galaxies.

nax cluster, which is estimated to reside ∼ 20 Mpc away (Tonry et al. 2001; Blakeslee et al. 2009; Tully et al. 2013; de Grijs & Bono 2020).

Table 1 contains the result from each galaxy, along with the halo and middle regions, where available. It lists the number of detected PNe ($N_{\rm PNe}$), as well as the number of expected PNe within 2.5 magnitudes of the PNLF cut-off ($N_{2.5}$). Errors on $N_{2.5}$ are derived on the basis of the Poisson uncertainties associated to the actual observed number of PNe $N_{\rm PNe}$, after rescaling. Here, we also present our best-fit values of $\mu_{\rm PNLF}$, and distance (in Mpc), as measured from the PNe populations. Table 1 also includes revised distance estimates for the FCC 167 and FCC 219 ($\mu_{\rm PNLF}$ = 31.30 ± 0.07 mag and 31.48 ± 0.10 mag, respectively) that are consistent with the values reported in S20 (31.24 ± 0.11 mag and 31.42 ± 0.10 mag), owing to the fact that in first place these objects have a fair number of PNe. For FCC 219, we also note the agreement between PNLF and TRGB method, where Hoyt et al. (2021) report a distance of 31.36 ± 0.04 ± 0.05 mag, which is within the uncertainty of our proposed $31.46^{+0.11}_{-0.12}$. In the case of FCC 167, Roth et al. (2021) have recently used the same MUSE data set to benchmark their refined 'on-off' band imaging PNe detection methodology, finding a smaller distance for FCC 167, with $\mu_{\rm PNLF}$ = 31.10 ± 0.04 mag. Although this comparison highlights a radial trend for the difference between our respective m_{5007} measurements, possibly due to some unaccounted stellar-population effect (which we limit through a de-

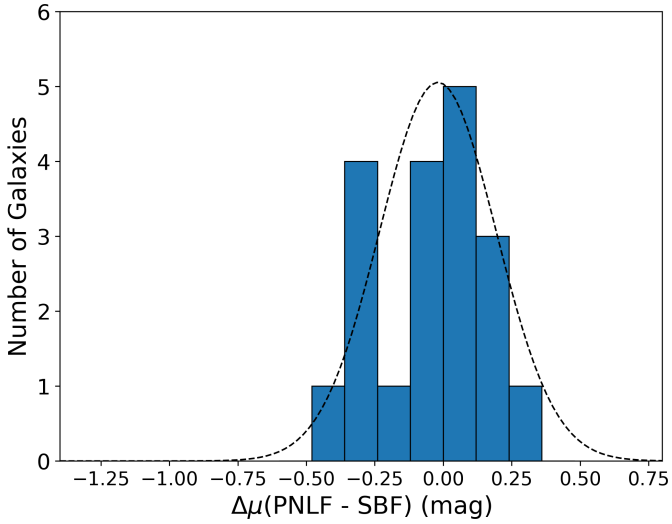

Fig. 5: Distribution of the difference ($\Delta\mu$) between our PNLF values of the distance modulus and those derived using SBF by Blakeslee et al. (2009). The $\Delta\mu$ distribution has a measured scatter of 0.21 mag around a median of 0.003 mag, as also shown by the reference Gaussian distribution with such median and standard deviation values. We adopt 0.12 mag bins to match Fig. 6 from Ciardullo (2012).

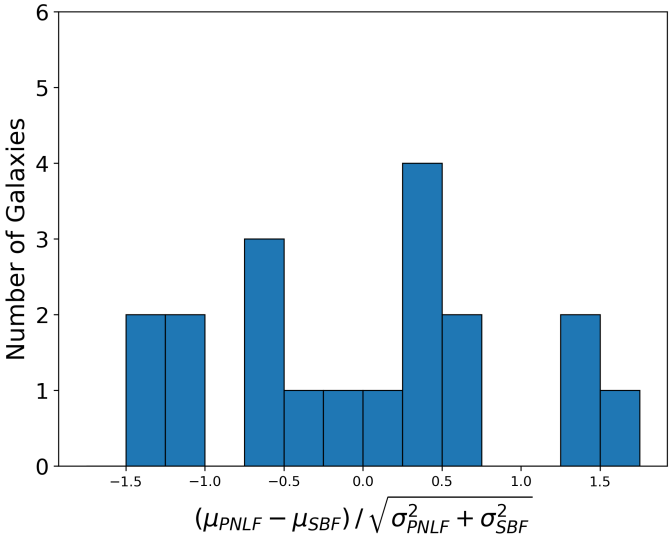

Fig. 6: Distribution for tension values between PNLF and SBF distance modulus. It results that 13 out of the 20 objects with both PNLF and SBF distance modulus show less than a 1σ tension between these measurements.

tailed spectral fitting), the origin for the distance offset appears to lie with the brightest PNe in the central pointing FCC 167, which all reside in low-stellar background regions. In this regime the simulations of S20 show that our m_{5007} measurements are rather robust, leaving room only for an offset in absolute flux calibration to explain the reported difference in the inferred distance. In this respect we avail of HST images to check the calibration of the MUSE data (see Sarzi et al. 2018, for details), which in the case of FCC 167 only required a 3% re-scaling towards lower fluxes (adding 0.03 mag). For what follows, we note that across our sample such a re-scaling averages out, indicating no systematic offset.

To validate our PNLF distance estimates, we started by comparing our individual to measurements to the SBF distances, which exist for all but one of our sample galaxies (FCC 161). Using the latest SBF values from either Blakeslee et al. (2009) or Blakeslee et al. (2010) (based on HST-ACS in the F850LP and F814W pass-band, respectively), Fig. 5 shows how overall our PNLF distances agree well with their SBF counterparts, with a median difference of $\Delta\mu = \mu_{\rm PNLF} - \mu_{\rm SBF} = 0.003$ mag and a standard deviation of 0.21 mag. In comparison, Ciardullo (2012) reported a median $\Delta\mu = -0.33$ mag corresponding to SBF distances being on average larger than PNLF estimates. Taking a step further, in Fig. 6 we show the distribution for the statistical tension between the PNLF and SBF distance measurements, dividing the $\Delta\mu$ values by the quadratic sum of their respective errors. Figure 6 further shows how our PNLF values agree on average with the SBF distances, with a large majority of cases showing less than a 1σ tension. How our PNLF distance measurements compare to the SBF estimates of Blakeslee et al. (2009) can be further appreciated in Fig. 7, where 15 of the 20 common objects indeed are consistent within the errors, as would be expected when adopting 1σ errors.

Of the galaxies covered here, we note the presence of three edge-on galaxies: FCC 153, FCC 170 and FCC 177. Both FCC 170, and FCC 177 measured $\mu_{\rm PNLF}$ show distinguished offsets from their SBF distance counterparts (Fig. 7). This would agree with both Blakeslee et al. (1999) and Mei et al. (2007), where the former reported differences between SBF distances and other distance methods for these objects, whereas the latter noted that SBF measurements for edge-on galaxies poses a greater challenge, compared to measurements with face-on galaxies. In fact, Ciardullo (2012) also remarks that the two galaxies that show the largest disagreement between SBF and PNLF distance measurements in their sample are edge-on. The disagreement between these two distance methods is believed, in part, to arise from the steeper gradient in stellar light along the line of sight of an edge-on galaxy, compared to the smoother stellar profile of a face-on galaxy.

Iodice et al. (2019a) find evidence of a potentially ongoing interaction between FCC 143 and FCC 147, from the Fornax Deep Survey (FDS, Iodice et al. 2019b) images. The Blakeslee et al. (2009) SBF distances indicate a separation of ~ 0.3 Mpc. We are at least able to confirm the distance of FCC 147 with a excellent agreement with the SBF measurement. However, the presence of only a handful of PNe within FCC 143 means that our distance estimate is no where near as reliable compared to that of FCC 147.

4.4. The distance to the Fornax cluster

Taking the weighted average of the PNLF derived distances, we estimate a distance to the Fornax cluster of 19.86 ± 0.32 Mpc. This is in remarkably good agreement, with similar uncertainties, with both 's SBF mean distance of 20.0 ± 0.3 ± 1.4 Mpc (Blakeslee et al. 2009) and recommended mean distance of $19.1^{+1.4}_{-1.2}$ Mpc, from Cepheid distances, SBF, and Tip of the Red Giant Branch (TRGB) methods (de Grijs & Bono 2020). Our reported average distance corresponds to a distance modulus of $\mu_{\rm PNLF} = 31.49 \pm 0.04$ mag and is based on all 21 ETGs listed in Table 1, whereas Blakeslee et al. (2009) report a median distance modulus to Fornax of $\mu_{\rm SBF} = 31.51 \pm 0.09$ mag based on over 43 objects they imaged with HST.

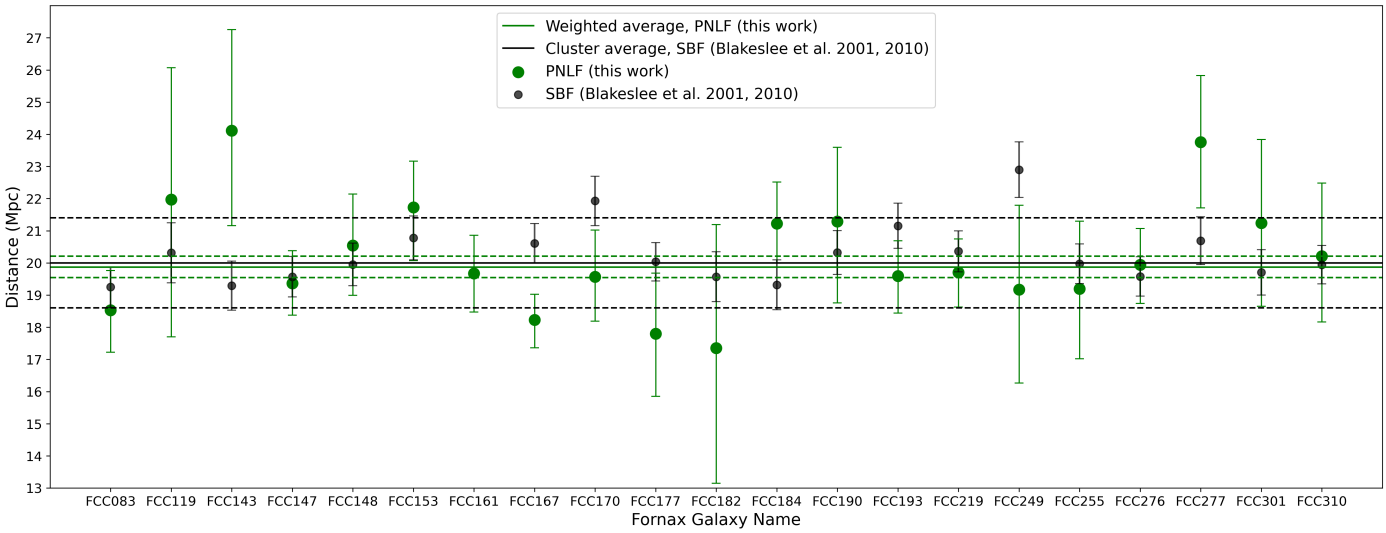

Fig. 7: Comparison between individual distance measurements (in Mpc) as obtained here using the PNLF (green circles and error bars) and as derived through SBF by Blakeslee et al. (2009, 2010). The solid and dashed green lines show the weighted average of our PNLF measurements and its associated error, as an estimate for the distance to the Fornax cluster. The black solid and dashed line indicate instead the SBF estimate distance to Fornax provided by Blakeslee et al. (2009) with its uncertainty, based on their entire sample of SBF distance measurements.

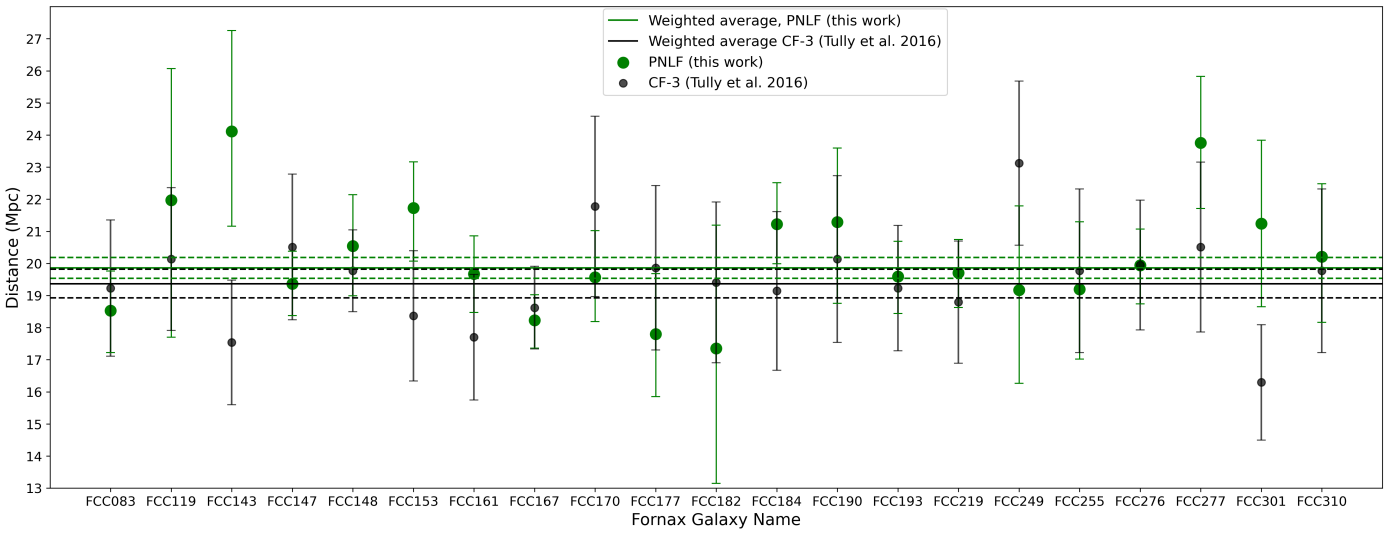

Fig. 8: Same as in to Fig. 7, but now comparing our PNLF distance estimates (green circles) with those reported in CosmicFlows-3 (Tully et al. 2016, black circles). The black solid and dotted lines show the weighted average and error from the CosmicFlows-3 data points.

To further gauge the reliability of our PNLF derived distances, Fig. 8 compares our values with those in the CosmicFlows-3 catalogue of Tully et al. (2016). This catalogue contains statistically derived mean values obtained combining published distances derived using Supernova Type Ia, the Fundamental Plane (FP), Globular Cluster Luminosity Function (GCLF), and the TRGB. As such measurements come with their own errors and potential biases, the values of CosmicFlows-3 catalogue show larger overall uncertainties compared to the SBF measurements of Blakeslee et al. (2009). Our PNLF values agree within the errors with the CosmicFlows-3 distances for all but two objects, providing further confidence also in the case of FCC 161 that was not targeted by Blakeslee et al. (2009). This is reflected also by the agreement between our PNLF average distance to Fornax and the value inferred using the CosmicFlows-3 value for our sample galaxies, which stands at 19.4 ± 0.4 Mpc ($\mu_{\rm PNLF}$= 31.44 ± 0.04 mag).

4.5. Fornax cluster spatial structure

Our PNLF distance measurements allows us to map out the ETG population of the Fornax cluster, comparing our independently derived distances within the cluster, and more specifically, to its brightest cluster galaxy (BCG); namely NGC 1399 (FCC 213). Here, we treat NGC 1399 as the central point of the cluster, with our ETGs situated around it. Before mapping the spatial distribution of our sample galaxies within the cluster, we first review the current distance estimates for NGC 1399.

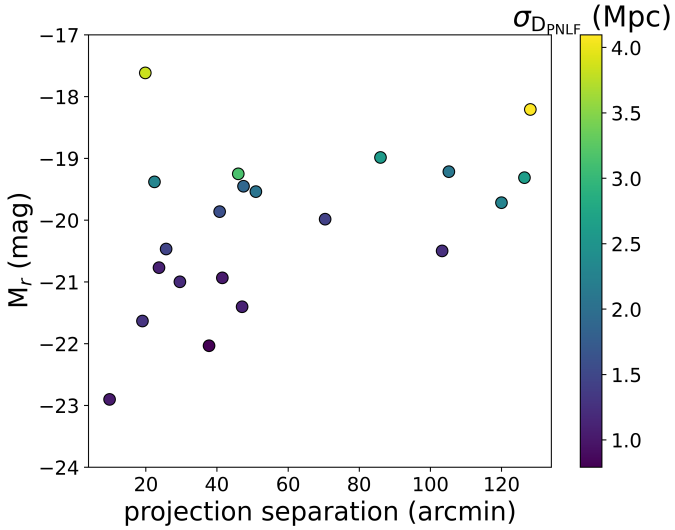

Fig. 9: Projected distance (in arcmin), from the BCG of the Fornax cluster NGC 1399, to the ETGs of our sample, as a function of their absolute *r*-band magnitude. Colour scale follows the calculated uncertainties in μ_{PNLF} for each galaxy. The r-band magnitudes are from Iodice et al. (2019b) except for FCC 119, FCC 249, and FCC 255, which we estimated to be 13.5, 12.1 and 12.2 mag respectively. This was obtained starting from the *B*-band magnitude reported in Sarzi et al. (2018) and by applying a colour-correction based on the spectral modelling of the integrated MUSE spectra for this target.

Blakeslee et al. (2009) reported a distance to NGC 1399 of 20.9 ± 0.9 Mpc, though this was updated to 21.1 ± 0.7 Mpc in Blakeslee et al. (2010). A few years earlier and always based on SBF, Tonry et al. (2001) measured a distance of 19.95 ± 1.47 Mpc. The CosmicFlows-3 survey reports a statistical mean distance from multiple sources of 22.08 ± 0.12 Mpc (Tully et al. 2013). MUSE data for NGC 1399 were collected both during the F3D survey, covering two external regions, and over the course of previous campaigns for the central regions (Prog. ID. 296.B-5054(A)). Upon reviewing these observations, which were taken under less than ideal seeing conditions compared to our other targets, we identified seven potential PNe in one of the F3D halo pointings. Initial estimates from converting the apparent magnitude of brightest PNe directly to the cut-off position produced an initial distance guess of ∼ 22 Mpc. Although this may agree with the results of Tully et al. (2013), the large uncertainties that would come with modelling such a sparse PNLF (∼0.45 mag, see Fig. 2) would not allow us to replace the previous other estimates for the distance to NGC 1399 nor provide a robust reference to help with the present discussion.

Though BCGs are expected to be close to the barycentre of a cluster, it is not always the case that they reside at the geometric centre of the cluster. NGC 1399 resides deep in the potential well of the cluster as traced by the X-ray emission of its hot intracluster gas, although the cluster itself comprises both of a main virialised region around NGC 1399 and of a secondary, offset group of in-falling objects around NGC 1316. In this respect, it is interesting to note how the Blakeslee et al. (2009, 2010) distance measurements for NGC 1399 would seeming place it not only behind the majority of our sample galaxies located within the virial radius of the Fornax cluster (according both to their and our PNLF measurements) but also beyond their own average distance to the cluster based also on objects further out. On the other hand, although the Tonry et al. (2001) distance for NGC 1399 comes with a larger error, it is closer to the average cluster distances presented in Blakeslee et al. (2010), Tully et al. (2013), and de Grijs & Bono (2020) as well as our own estimate for Fornax cluster distance. It would therefore seem a more indicative distance to NGC 1399 and the barycentre of the Fornax cluster.

Another expectation for the structure of a galaxy cluster is mass segregation as a result of dynamical friction, in particular for less massive clusters where tidal stripping cannot act as an obstacle to mass segregation as it does in the most massive ones (see, e.g. Kim et al. 2020). To start investigating whether that happened in Fornax, in Fig. 9 we show the tangential separation of each galaxy from NGC 1399 compared to their *r*-band absolute magnitude (Iodice et al. 2019b), used as proxy for their mass. As projected on the sky, the majority of galaxies reside within 1 degree separation, with the uncertainty in their PNLF distance decreasing with brighter *r*-band magnitudes. To a first order, the more luminous and massive galaxies appear closer to the expected cluster centre (i.e. NGC 1399), with less luminous objects being more spread out in projected sky separation. To more accurately depict the 3D structure of the Fornax cluster, we compare the spatial distances between each galaxy to NGC 1399, against their absolute *r*-band magnitude.

Considering both the distance estimate to NGC 1399 of Blakeslee et al. (2010) and Tonry et al. (2001), in Fig. 10 we produce three different scenarios for the spatial distribution of the ETGs covered here. The first panel (left), compares the distances taken from Blakeslee et al. (2009, 2010) to their own distance of 21.1 Mpc for NGC 1399 (Blakeslee et al. 2010). The galaxies are scattered between 0.5 and 2.1 Mpc, with little indication for a trend with absolute *r*-band magnitude. The second panel (middle) compares the SBF distances of Blakeslee et al. (2009) against the NGC 1399 distance of 19.95 Mpc (Tonry et al. 2001). In contrast to the first panel, we find that the majority of galaxies are concentrated within 1 Mpc of NGC 1399. The final panel (right) compares our PNLF distances to the Tonry et al. (2001) NGC 1399 distance. Here, we find that, again, the majority of galaxies reside within 1.5 Mpc, though we also note some galaxies showing a separation of ∼ 2.5 Mpc. Although in this case we note that the brightest object is closer to NGC1399, overall from these comparisons we do not find clear evidence of mass segregation within the virial radius of the Fornax Cluster, in particular when we consider the large uncertainties in projected PNLF distance, which would correspond to similarly wide errors in the 3D separation.

4.6. Planetary nebulae sample sizes across the cluster

The accuracy of our PNLF distance measurement depends primarily on the PNe sample size, which in turn for a simple and relatively old stellar population is expected to simply scale with the luminosity of that population (Renzini & Buzzoni 1986). For our sample of ETGs this is confirmed by trend shown in Fig. 11, between the *r*-band magnitude corresponding to the stellar flux encompassed by our single F3D pointings (without accounting regions excluded in our PNe analysis) and the expected number of PNe within 2.5 magnitudes from the bright cut-off of the PNLF, as inferred from our best match to the observed PNLF in these same pointings. Much of the scatter in the observed trend can be explained by the varying imaging quality underlying our PNLF measurements, whereby a broader PSF lead to less PNe being detected and to a larger uncertainty in the inferred intrinsic number of PNe. Other factors may also be at work, however,

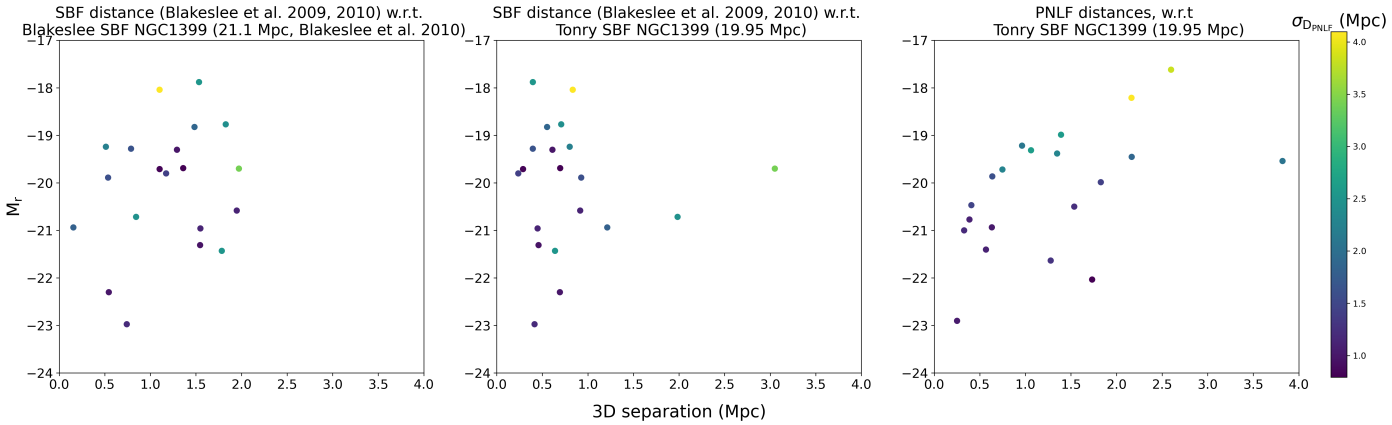

Fig. 10: Comparison between the distance (in Mpc) from NGC 1399 of our sample galaxies versus their absolute *r*-band magnitude, using different sources for the distance estimates to our sample galaxies and NGC 1399. Left panel: adopting the Blakeslee et al. (2009) distances to the individual F3D galaxies and the Blakeslee et al. (2010) distance to NGC 1399 (21.1Mpc). Middle panel: same as in the left panel but using the SBF distance to NGC 1399 derived by Tonry et al. (2001, 19.95 Mpc). Right panel: Still using the Tonry et al. distance to NGC 1399 but using our PNLF-derived distances to our sample galaxies. The *r*-band magnitudes are from Iodice et al. (2019b) except for FCC 119, FCC 249, and FCC 255, which are estimated to be 13.5, 12.1 and 12.2 mag respectively.

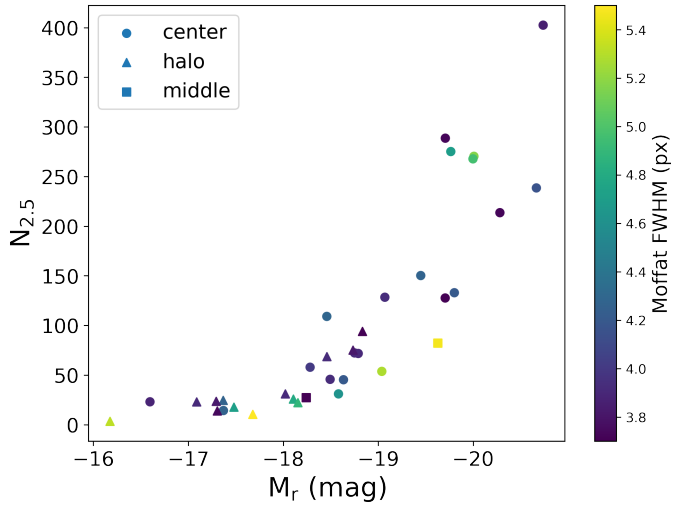

Fig. 11: Number of expected PNe within each galaxy pointing (Table 1) plotted against their *r*-band absolute magnitude, as derived from the MUSE data covering exactly the same regions within each pointing where the presence of PNe is investigated, thus excluding masked out regions. Different symbols denote central, middle, and halo pointing, and the colour-coding indicates the FWHM value of our Moffat PSF model, as derived within each pointing through the simultaneous fit of the brightest PNe.

such a dependency with stellar metallicity for the specific number of PNe (Buzzoni et al. 2006) leading to more PNe rich population in metal regions, as would be probed better by our middle or halo pointing in the case of large objects. Following the efforts of Martín-Navarro et al. (2019), Martin-Navarro et al. (2021, in prep) now presents stellar-population parameter maps for the entire, which provides a strong basis to further investigate the link between PNe and their parent populations in a future paper.

5. Conclusions

Extending the work of Spriggs et al. (2020) to the full sample of ETGs targeted by the Fornax3D survey we have presented a catalogue of 1350 unique PNe sources across 21 different objects. The catalogue includes the PNe positions, their [O III] 5007 Å flux and LOSV, with the PNe population of each galaxy being catalogued in standardised tables, available online: Tables A.1 to A.36 .

Using the luminosity function observed in each galaxy (limited to the central pointing for larger objects) we have have derived independent distance estimates by matching such PNLFs across their entire magnitude range thanks to a careful treatment of the PNe detection incompleteness. Using simulations we have checked the behaviour of our estimated distance errors and demonstrated that our PNLF distance estimates remain unbiased even when based on a low number of PNe. Furthermore, although the present data do not allow one to set meaningful constraints on the shape of the PNLF, as characterised by the generalised form introduced by Longobardi et al. (2013), our methods are capable of detecting possible variations for PNe sample sizes not too far from the one we presently obtained.

Our PNLF distance estimate are generally consistent within the errors with distances derived using SBF (Blakeslee et al. 2009, 2010) or through the combination of various methods other than PNLF (Tully et al. 2013, 2016). In the case of SBF, on average our PNLF distance modulii closely match the SBF values, thus appearing to largely reduce previous tensions between these two methodologies.

With PNLF distances for 21 ETGs within the virial radius of the Fornax cluster we estimated a weighted average distance to Fornax of 19.86 ± 0.32 Mpc. This is consistent within the errors with the distance to this cluster derived from SBF values for all 43 ETGs observed Blakeslee et al. (2009, 20 Mpc) across the whole cluster and the one recommended by de Grijs & Bono (2020, 19.1 Mpc) combining a variety of methods.

We also investigated the spatial distribution of the ETGs of the F3D survey, in particular in relation to the BCG NGC 1399. Though we do not produce our own distance to this BCG, we review different cluster structure scenarios that arise from

the NGC 1399 SBF distances of Blakeslee et al. (2009, 2010) and Tonry et al. (2001), corresponding to 21.1 Mpc and 19.95 Mpc, respectively. Assuming the Blakeslee et al. (2010) value, NGC 1399 would be behind most of the objects we observe and ∼1 Mpc further than the average SBF distance provided by Blakeslee et al. (2009) for the Fornax cluster. On the other hand, that the SBF distance to NGC 1399 of Tonry et al. (2001) agrees better with Blakeslee et al. (2009) distance to Fornax and the average PNLF distance provided by our objects inside the virial radius. This is consistent with the expectation that NGC 1399 is well centred on the potential well of the Fornax cluster, as traced also by the distribution of the hot intracluster medium. Mass segregation should be facilitated in a relatively modest cluster such as Fornax, but we found no strong evidence for it, independent of the assumed distance to NGC 1399 and whether we used SBF of PNLF distances. More accurate distance estimates will be needed to further explore the 3D structure of Fornax and other nearby clusters.

The present catalogue will be of great values for future investigation of the central PNe populations of ETGs, in particular in relation to the properties of their parent stellar population. The MUSE data at hand will allow us to measure stellar age, metallicity, α-element abundance (Martín-Navarro et al. 2019), and the star-formation history (Pinna et al. 2019b,a) of the stellar population in our sample galaxies in the same regions where our PNe are detected. Using this information, we explore in particular how the luminosity specific number of PNe $\alpha_{2.5}$ derived here will vary across the sample as a function of of these stellar population properties, in addition to measurements for the near and far-UV continuum, testing the results of previous comparisons (e.g. Buzzoni et al. 2006).

To conclude, we note the exciting prospects performing adaptive-optics (AO) observations with MUSE observations for the purpose of exploring the PNe population of nearby galaxies. Indeed, if present seeing-limited MUSE data allow one to detect PNe and measure PNLF distances out to a distance of 20 Mpc, finding over a hundred of PNe in the most massive objects and thus measuring distances within a 5% accuracy (see also S20 Roth et al. 2021), AO-assisted observations have the potential to at least double the reachable distance with the PNLF method. This can be understood considering that whereas the background noise in the MUSE observations is not set to vary dramatically for objects further out (owing to how surface brightness is conserved with distance), AO-observations delivering a 0.4″wide point-spread function instead of the 0.8″width (typical for good-seeing conditions at Paranal) will lead to a four-fold increase in the central [O III] 5007 Å peak flux and spectral amplitude, thus compensating for the flux attenuation observed for PNe twice as further away. By the same token, AO-observations of objects as far away as Virgo or Fornax will allow one to reach −1.5 mag further down from the PNLF bright cut-off, making it possible to further test the universality of the PNLF and better understand its origin.

Acknowledgements. We would like to thank the referee for their constructive responses, which helped to improved the content and clarity of this manuscript. Based on observations collected at the European Southern Observatory under ESO pro-gramme 296.B-5054(A). TS thanks R. Jackson, S. Kaviraj and A. Bittner for their help and ideas that aided in the construction and presentation of this paper. This work was supported by Science and Technology Facilities Council [grant number ST/R504786/1]. GvdV acknowledges funding from the European Research Council (ERC) under the European Union's Horizon 2020 research and innovation programme under grant agreement No 724857 (Consolidator Grant ArcheoDyn). RMcD acknowledges financial support as a recipient of an Australian Research Council Future Fellowship (project number FT150100333). J. F-B and I. M-N acknowledge support through the RAVET project by the grant PID2019-107427GB-C32 from the Spanish Ministry of Science, Innovation and Universities (MCIU), and through the IAC project TRACES which is partially supported through the state budget and the regional budget of the Consejería de Economía, Industria, Comercio y Conocimiento of the Canary Islands Autonomous Community. FP acknowledges support from grant PID2019-107427GB-C32 from The Spanish Ministry of Science and Innovation. EMC acknowledges support by Padua University grants DOR1885254/18, DOR1935272/19, and DOR2013080/20 and by MIUR grant PRIN 2017 20173ML3WW_001. This project made use of the following software packages: LMfit (Newville et al. 2014, 2019), Astropy, a community-developed core Python package for Astronomy (Robitaille et al. 2013), scipy (Eric Jones and Travis Oliphant and Pearu Peterson and et al. 2001), Numpy (Van Der Walt et al. 2011), matplotlib (Hunter 2007) and Pandas (Mckinney 2010).

References

Bacon, R., Accardo, M., Adjali, L., et al. 2010, in Ground-based and Airborne Instrumentation for Astronomy III, ed. I. S. McLean, S. K. Ramsay, & H. Takami, Vol. 7735, 773508
Bhattacharya, S., Arnaboldi, M., Caldwell, N., et al. 2019a, Astronomy and Astrophysics, 631, A56
Bhattacharya, S., Arnaboldi, M., Gerhard, O., et al. 2021, Astronomy and Astrophysics, 647, A130
Bhattacharya, S., Arnaboldi, M., Hartke, J., et al. 2019b, Astronomy and Astrophysics, 624, A132
Bittner, A., Falcón-Barroso, J., Nedelchev, B., et al. 2019, Astronomy & Astrophysics, 628, A117, publisher: EDP Sciences
Blakeslee, J. P., Ajhar, E. A., & Tonry, J. L. 1999, 237, 181, conference Name: Post-Hipparcos Cosmic Candles Place: eprint: arXiv:astro-ph/9807124
Blakeslee, J. P., Cantiello, M., Mei, S., et al. 2010, The Astrophysical Journal, 724, 657
Blakeslee, J. P., Jordán, A., Mei, S., et al. 2009, The Astrophysical Journal, 694, 556
Buzzoni, A., Arnaboldi, M., & Corradi, R. L. M. 2006, Monthly Notices of the Royal Astronomical Society, 368, 877
Cappellari, M. 2017, Monthly Notices of the Royal Astronomical Society, 466, 798
Cappellari, M. & Emsellem, E. 2004, Publications of the Astronomical Society of the Pacific, 116, 138, iSBN: 0300104251
Ciardullo, R. 2012, Astrophysics and Space Science, 341, 151
Ciardullo, R., Jacoby, G. H., & Ford, H. C. 1989a, The Astrophysical Journal, 344, 715
Ciardullo, R., Jacoby, G. H., Ford, H. C., & Neill, J. D. 1989b, The Astrophysical Journal, 339, 53
Ciardullo, R., Jacoby, G. H., & Tonry, J. L. 1993, The Astrophysical Journal, 419, 479
Coccato, L., Gerhard, O., Arnaboldi, M., et al. 2009, Monthly Notices of the Royal Astronomical Society, 394, 1249
de Grijs, R. & Bono, G. 2020, The Astrophysical Journal Supplement Series, 246, 3
Douglas, N. G., Napolitano, N. R., Romanowsky, A. J., et al. 2007, The Astrophysical Journal, 664, 257, publisher: IOP Publishing
Eric Jones and Travis Oliphant and Pearu Peterson and et al. 2001, SciPy: Open Source Scientific Tools for Python
Fahrion, K., Lyubenova, M., van de Ven, G., et al. 2019, Astronomy & Astrophysics, 628, A92
Feldmeier, J. J., Jacoby, G. H., & Phillips, M. M. 2007, The Astrophysical Journal, 657, 76
Freudling, W., Romaniello, M., Bramich, D. M., et al. 2013, A&A, 559, A96
Galán-de Anta, P. M., Sarzi, M., Spriggs, T. W., et al. 2021, arXiv e-prints, arXiv:2106.11657
Gerhard, O., Arnaboldi, M., Freeman, K. C., et al. 2005, The Astrophysical Journal Letters, 621, L93
Hartke, J., Arnaboldi, M., Longobardi, A., et al. 2017, Astronomy and Astrophysics, 603, A104
Hernández-Martínez, L. & Peña, M. 2009, Astronomy and Astrophysics, 495, 447
Herrmann, K. A., Ciardullo, R., Feldmeier, J. J., & Vinciguerra, M. 2008, The Astrophysical Journal, 683, 630
Hoyt, T. J., Beaton, R. L., Freedman, W. L., et al. 2021, The Astrophysical Journal, 915, 34
Hunter, J. D. 2007, Computing in Science and Engineering, 9, 99
Iodice, E., Sarzi, M., Bittner, A., et al. 2019a, A&A, 627, A136, publisher: EDP Sciences
Iodice, E., Spavone, M., Capaccioli, M., et al. 2019b, A&A, 623, A1
Jacoby, G. H. 1989, The Astrophysical Journal, 339, 39

Jacoby, G. H., Ciardullo, R., De Marco, O., et al. 2013, The Astrophysical Journal, 769, 10
Jacoby, G. H., Ciardullo, R., Ford, H. C., & Booth, J. 1989, The Astrophysical Journal, 344, 704
Jacoby, G. H. & De Marco, O. 2002, The Astronomical Journal, 123, 269
Kafle, P. R., Sharma, S., Lewis, G. F., Robotham, A. S. G., & Driver, S. P. 2018, Monthly Notices of the Royal Astronomical Society, 475, 4043, publisher: Oxford University Press
Kim, S., Contini, E., Choi, H., et al. 2020, The Astrophysical Journal, 905, 12
Kreckel, K., Groves, B., Bigiel, F., et al. 2017, The Astrophysical Journal, 834, 174
Longobardi, A., Arnaboldi, M., Gerhard, O., et al. 2013, Astronomy and Astrophysics, 558, A42
Longobardi, A., Arnaboldi, M., Gerhard, O., Pulsoni, C., & Söldner-Rembold, I. 2018, Astronomy and Astrophysics, 620, publisher: EDP Sciences
Martin, T. B., Drissen, L., & Melchior, A.-L. 2018, Monthly Notices of the Royal Astronomical Society, 473, 4130
Martín-Navarro, I., Lyubenova, M., van de Ven, G., et al. 2019, Astronomy and Astrophysics, 626, A124
Mckinney, W. 2010, Data Structures for Statistical Computing in Python, Tech. rep., AQR Capital Management, publication Title: PROC. OF THE 9th PYTHON IN SCIENCE CONF
McMillan, R., Ciardullo, R., & Jacoby, G. H. 1993, The Astrophysical Journal, 416, 62
Mei, S., Blakeslee, J. P., Côté, P., et al. 2007, The Astrophysical Journal, 655, 144
Merrett, H. R., Merrifield, M. R., Douglas, N. G., et al. 2006, Monthly Notices of the Royal Astronomical Society, 369, 120
Nelder, J. A. & Mead, R. 1965, The Computer Journal, 7, 308
Newville, M., Otten, R., Nelson, A., et al. 2019, lmfit/lmfit-py 1.0.0, Tech. rep., University of Chicago
Newville, M., Stensitzki, T., Allen, D. B., & Ingargiola, A. 2014, LMFIT: Non-Linear Least-Square Minimization and Curve-Fitting for Python\P, Tech. rep., University of Chicago
Pastorello, N., Sarzi, M., Cappellari, M., et al. 2013, Monthly Notices of the Royal Astronomical Society, 430, 1219
Pinna, F., Falcón-Barroso, J., Martig, M., et al. 2019a, Astronomy and Astrophysics, 625, A95
Pinna, F., Falcón-Barroso, J., Martig, M., et al. 2019b, Astronomy and Astrophysics, 623, A19
Pulsoni, C., Gerhard, O., Arnaboldi, M., et al. 2018, Astronomy and Astrophysics, 618, A94
Renzini, A. & Buzzoni, A. 1986, Spectral Evolution of Galaxies, 122, 195
Robitaille, T. P., Tollerud, E. J., Greenfield, P., et al. 2013, Astronomy and Astrophysics, 558
Romanowsky, A. J., Douglas, N. G., Arnaboldi, M., et al. 2003, Science, 301, 1696
Roth, M. M., Jacoby, G. H., Ciardullo, R., et al. 2021, arXiv e-prints, 2105, arXiv:2105.01982
Sarzi, M., Iodice, E., Coccato, L., et al. 2018, Astronomy and Astrophysics, 616, A121
Spriggs, T. & gdapablo. 2021, tspriggs/MUSE_PNe_fitting: Planetary Nebulae analysis within MUSE data - update
Spriggs, T. W., Sarzi, M., Napiwotzki, R., et al. 2020, A&A, 637, A62, publisher: EDP Sciences
Teodorescu, A. M., Méndez, R. H., Saglia, R. P., et al. 2005, The Astrophysical Journal, 635, 290
Tonry, J. L., Dressler, A., Blakeslee, J. P., et al. 2001, The Astrophysical Journal, 546, 681
Tully, R. B., Courtois, H. M., Dolphin, A. E., et al. 2013, The Astronomical Journal, 146, 86
Tully, R. B., Courtois, H. M., & Sorce, J. G. 2016, The Astronomical Journal, 152, 50
Van Der Walt, S., Colbert, S. C., & Varoquaux, G. 2011, Computing in Science and Engineering, 13, 22
Vazdekis, A., Koleva, M., Ricciardelli, E., Röck, B., & Falcón-Barroso, J. 2016, Monthly Notices of the Royal Astronomical Society, 463, 3409, publisher: Oxford University Press
Vazdekis, A., Ricciardelli, E., Cenarro, A. J., et al. 2012, Monthly Notices of the Royal Astronomical Society, 424, 157
Weilbacher, P. M., Streicher, O., & Palsa, R. 2016, Astrophysics Source Code Library, ascl:1610.004
Weilbacher, P. M., Streicher, O., Urrutia, T., et al. 2012, in Software and Cyberinfrastructure for Astronomy II, ed. N. M. Radziwill & G. Chiozzi, Vol. 8451, 84510B

Appendix A: PNe Catalogue

Table A.1: Central PNe of FCC 083

Source ID	RA (J2000)	Dec (J2000)	m_{5007}	σm_{5007}	A/rN	LOSV km s^{-1}	σ LOSV	label	index
F3D J033035.64-345145.52	03h30m35.64s	-34d51m45.52s	28.08	0.06	4.9	1356.5	4.4	PN	C-1
F3D J033035.95-345142.83	03h30m35.95s	-34d51m42.83s	28.39	0.07	4.2	1566.9	5.6	PN	C-2
F3D J033032.68-345140.24	03h30m32.68s	-34d51m40.24s	28.09	0.09	4.0	1535.9	7.6	PN	C-3
F3D J033036.38-345138.89	03h30m36.38s	-34d51m38.89s	28.0	0.05	6.1	1495.4	3.8	PN	C-4
F3D J033034.30-345138.50	03h30m34.30s	-34d51m38.50s	28.53	0.07	3.9	1671.2	5.7	PN	C-5
F3D J033035.98-345136.52	03h30m35.98s	-34d51m36.52s	28.25	0.06	5.1	1278.9	4.9	PN	C-6
F3D J033036.85-345131.73	03h30m36.85s	-34d51m31.73s	27.48	0.05	9.8	1358.2	2.2	PN	C-7
F3D J033033.65-345131.27	03h30m33.65s	-34d51m31.27s	27.44	0.04	11.0	1475.4	2.1	PN	C-8
F3D J033033.54-345131.08	03h30m33.54s	-34d51m31.08s	27.58	0.05	10.1	1550.3	2.4	PN	C-9
F3D J033033.16-345130.64	03h30m33.16s	-34d51m30.64s	27.0	0.04	17.6	1638.3	1.4	PN	C-10
F3D J033034.57-345129.77	03h30m34.57s	-34d51m29.77s	28.34	0.07	4.2	1495.5	5.7	PN	C-11
F3D J033036.82-345128.18	03h30m36.82s	-34d51m28.18s	27.41	0.05	9.9	1429.7	2.5	PN	C-12
F3D J033035.26-345125.84	03h30m35.26s	-34d51m25.84s	27.65	0.06	5.8	1480.7	4.0	PN	C-13
F3D J033036.61-345125.54	03h30m36.61s	-34d51m25.54s	27.84	0.05	6.8	1527.5	3.6	PN	C-14
F3D J033034.60-345124.13	03h30m34.60s	-34d51m24.13s	27.16	0.05	9.9	1571.7	2.3	PN	C-15
F3D J033036.31-345123.58	03h30m36.31s	-34d51m23.58s	28.27	0.07	4.3	1446.9	5.7	PN	C-16
F3D J033035.57-345123.23	03h30m35.57s	-34d51m23.23s	27.78	0.06	4.7	1484.7	5.1	PN	C-17
F3D J033033.05-345122.68	03h30m33.05s	-34d51m22.68s	28.35	0.06	5.1	1667.5	4.9	PN	C-18
F3D J033035.27-345121.94	03h30m35.27s	-34d51m21.94s	27.37	0.05	6.2	1433.6	3.9	PN	C-19
F3D J033032.26-345121.63	03h30m32.26s	-34d51m21.63s	28.44	0.06	4.7	1665.4	4.7	PN	C-20
F3D J033035.26-345120.23	03h30m35.26s	-34d51m20.23s	27.61	0.07	4.1	1484.5	5.6	PN	C-21
F3D J033035.56-345119.97	03h30m35.56s	-34d51m19.97s	27.79	0.06	4.3	1584.0	5.4	PN	C-22
F3D J033034.16-345119.00	03h30m34.16s	-34d51m19.00s	27.2	0.05	10.2	1419.3	2.3	PN	C-23
F3D J033035.50-345117.22	03h30m35.50s	-34d51m17.22s	27.84	0.07	3.7	1439.9	6.4	PN	C-24
F3D J033036.50-345116.67	03h30m36.50s	-34d51m16.67s	28.06	0.06	6.0	1459.8	4.0	PN	C-25
F3D J033034.23-345115.74	03h30m34.23s	-34d51m15.74s	27.71	0.06	5.8	1825.9	4.2	PN	C-26
F3D J033035.83-345115.12	03h30m35.83s	-34d51m15.12s	27.42	0.05	7.9	1605.9	3.1	PN	C-27
F3D J033036.09-345114.61	03h30m36.09s	-34d51m14.61s	27.93	0.06	5.6	1411.0	4.1	PN	C-28
F3D J033035.76-345112.37	03h30m35.76s	-34d51m12.37s	28.08	0.07	4.3	1488.9	5.6	PN	C-29
F3D J033036.67-345112.81	03h30m36.67s	-34d51m12.81s	26.79	0.04	19.1	1540.4	1.3	PN	C-30
F3D J033033.53-345110.09	03h30m33.53s	-34d51m10.09s	27.84	0.05	6.3	1689.8	3.8	PN	C-31
F3D J033034.46-345109.19	03h30m34.46s	-34d51m09.19s	27.21	0.05	6.8	1728.8	3.5	PN	C-32
F3D J033034.00-345110.54	03h30m34.00s	-34d51m10.54s	26.97	0.04	11.6	1469.3	2.2	imp	C-33
F3D J033034.06-345109.93	03h30m34.06s	-34d51m09.93s	27.35	0.05	10.5	1472.6	2.5	PN	C-34
F3D J033034.18-345109.27	03h30m34.18s	-34d51m09.27s	27.91	0.06	4.4	1497.8	5.4	PN	C-35
F3D J033033.99-345108.96	03h30m33.99s	-34d51m08.96s	27.72	0.05	5.9	1520.4	3.7	PN	C-36
F3D J033034.72-345108.46	03h30m34.72s	-34d51m08.46s	27.07	0.05	6.8	1684.3	3.6	PN	C-37
F3D J033037.25-345107.61	03h30m37.25s	-34d51m07.61s	28.58	0.07	3.6	1426.4	6.4	PN	C-38
F3D J033034.41-345107.57	03h30m34.41s	-34d51m07.57s	26.94	0.05	9.6	1659.1	2.5	PN	C-39
F3D J033033.90-345107.03	03h30m33.90s	-34d51m07.03s	28.07	0.06	4.6	1546.0	5.3	PN	C-40
F3D J033033.13-345106.98	03h30m33.13s	-34d51m06.98s	28.47	0.07	4.1	1655.4	5.8	PN	C-41
F3D J033034.79-345106.58	03h30m34.79s	-34d51m06.58s	27.64	0.06	4.5	1707.8	4.9	PN	C-42
F3D J033034.16-345106.30	03h30m34.16s	-34d51m06.30s	27.7	0.06	5.5	1603.0	4.4	PN	C-43
F3D J033035.26-345106.09	03h30m35.26s	-34d51m06.09s	27.73	0.06	5.3	1591.8	4.6	PN	C-44
F3D J033034.90-345106.01	03h30m34.90s	-34d51m06.01s	27.65	0.06	4.6	1664.5	4.9	PN	C-45
F3D J033034.62-345105.85	03h30m34.62s	-34d51m05.85s	27.58	0.06	5.2	1690.3	4.6	PN	C-46
F3D J033033.70-345105.61	03h30m33.70s	-34d51m05.61s	27.66	0.05	7.1	1450.5	3.2	PN	C-47
F3D J033034.78-345103.77	03h30m34.78s	-34d51m03.77s	27.9	0.07	4.3	1660.1	5.4	PN	C-48
F3D J033035.43-345103.45	03h30m35.43s	-34d51m03.45s	27.96	0.06	5.1	1538.5	4.5	PN	C-49
F3D J033035.27-345103.52	03h30m35.27s	-34d51m03.52s	27.74	0.06	5.7	1516.3	4.1	PN	C-50
F3D J033037.40-345102.78	03h30m37.40s	-34d51m02.78s	27.28	0.05	9.5	1440.3	2.4	PN	C-51

Table A.1: FCC 083 continued

Source ID	RA (J2000)	Dec (J2000)	m_{5007}	σm_{5007}	A/rN	LOSV km s^{-1}	σ LOSV	label	index
F3D J033035.99-345102.53	03h30m35.99s	-34d51m02.53s	28.52	0.07	3.7	1529.0	6.2	PN	C-52
F3D J033034.23-345102.49	03h30m34.23s	-34d51m02.49s	28.37	0.08	3.1	1430.3	7.5	PN	C-53
F3D J033035.57-345058.71	03h30m35.57s	-34d50m58.71s	27.52	0.05	9.1	1455.8	2.6	PN	C-54
F3D J033034.82-345058.16	03h30m34.82s	-34d50m58.16s	27.99	0.06	5.2	1483.0	4.5	PN	C-55
F3D J033033.74-345056.72	03h30m33.74s	-34d50m56.72s	28.54	0.08	3.4	1778.5	7.1	PN	C-56
F3D J033034.37-345056.12	03h30m34.37s	-34d50m56.12s	27.33	0.05	9.7	1690.7	2.5	PN	C-57
F3D J033033.01-345054.73	03h30m33.01s	-34d50m54.73s	28.74	0.08	3.3	1624.3	7.0	PN	C-58
F3D J033033.72-345054.61	03h30m33.72s	-34d50m54.61s	27.67	0.05	7.8	1642.6	3.2	PN	C-59
F3D J033035.75-345054.00	03h30m35.75s	-34d50m54.00s	28.31	0.06	5.0	1526.8	4.5	PN	C-60
F3D J033034.42-345053.77	03h30m34.42s	-34d50m53.77s	28.49	0.07	3.8	1649.7	6.3	PN	C-61
F3D J033035.73-345049.49	03h30m35.73s	-34d50m49.49s	28.08	0.05	6.1	1571.7	3.5	PN	C-62
F3D J033032.92-345044.44	03h30m32.92s	-34d50m44.44s	28.82	0.08	3.2	1562.4	7.3	PN	C-63

Notes. PNe catalogue for the FCC 083 central region: 'Source ID' (using the IAU standard, with the F3D prefix), 'RA (J2000)' and 'Dec (J2000)', 'm_{5007}' as magnitude in [O III] 5007Å, 'A/rN' for the signal-to-residual noise, 'LOSV (km s^{-1})' for the observed LOS velocity (km s^{-1}) and label each source under 'Identifier' with the appropriate label: PNe, SNR, H II, OvLu (over-luminous), or Interl (interloper).

Table A.2: Halo PNe of FCC 083

Source ID	RA (J2000)	Dec (J2000)	m_{5007}	σm_{5007}	A/rN	LOSV km s^{-1}	σ LOSV	label	index
F3D J033033.89-345106.66	03h30m33.89s	-34d51m06.66s	28.27	0.17	3.6	1549.5	5.5	PN	H-1 / C-42
F3D J033033.69-345105.63	03h30m33.69s	-34d51m05.63s	27.99	0.17	5.3	1455.7	3.4	PN	H-2 / C-49
F3D J033031.81-345101.88	03h30m31.81s	-34d51m01.88s	28.32	0.17	5.3	1682.5	3.4	PN	H-3
F3D J033032.25-345058.51	03h30m32.25s	-34d50m58.51s	28.71	0.17	3.9	1618.3	4.9	PN	H-4
F3D J033032.99-345054.71	03h30m32.99s	-34d50m54.71s	28.75	0.17	3.7	1643.4	4.9	PN	H-5 / C-61
F3D J033033.72-345054.66	03h30m33.72s	-34d50m54.66s	27.81	0.17	8.2	1651.2	2.3	PN	H-6 / C-62
F3D J033033.75-345056.63	03h30m33.75s	-34d50m56.63s	28.44	0.17	4.4	1783.5	4.4	PN	H-7 / C-59
F3D J033031.58-345041.48	03h30m31.58s	-34d50m41.48s	27.98	0.17	8.0	1549.0	2.4	PN	H-8
F3D J033029.66-345037.11	03h30m29.66s	-34d50m37.11s	28.1	0.17	6.9	1695.5	2.7	PN	H-9
F3D J033030.57-345032.60	03h30m30.57s	-34d50m32.60s	28.66	0.17	5.1	1597.1	3.7	PN	H-10
F3D J033033.95-345031.17	03h30m33.95s	-34d50m31.17s	28.1	0.17	7.1	1703.1	2.6	PN	H-11
F3D J033031.87-345029.64	03h30m31.87s	-34d50m29.64s	28.98	0.17	3.5	1699.2	5.5	PN	H-12
F3D J033032.94-345027.21	03h30m32.94s	-34d50m27.21s	27.45	0.17	12.9	1469.7	1.5	PN	H-13
F3D J033033.94-345026.15	03h30m33.94s	-34d50m26.15s	28.96	0.17	3.6	1644.8	5.1	PN	H-14
F3D J033034.22-345018.64	03h30m34.22s	-34d50m18.64s	27.54	0.17	13.8	1628.5	1.4	PN	H-15
F3D J033032.06-345016.72	03h30m32.06s	-34d50m16.72s	28.4	0.17	6.1	1717.4	3.0	PN	H-16
F3D J033033.11-345014.43	03h30m33.11s	-34d50m14.43s	28.19	0.17	7.4	1629.6	2.6	PN	H-17
F3D J033034.67-345009.13	03h30m34.67s	-34d50m09.13s	28.81	0.17	3.3	1563.8	5.6	PN	H-18
F3D J033032.84-345008.18	03h30m32.84s	-34d50m08.18s	28.51	0.17	4.8	1653.0	4.0	PN	H-19

Notes. Halo: Source catalogue for FCC 083: Source ID (using the IAU standard, with the F3D prefix), RA and Dec, magnitude in [O III] 5007Å, signal-to-residual noise, observed LOS velocity (kms^{-1}) and object label (PNe, SNR, H II, OvLu (over-luminous), or Interl (interloper). This also an example of the rest of the Fornax PNe catalogues presented here.

Appendix B: Simulations for optimising both $\mu_{\rm PNLF}$ and c_2

By exploiting the entire range of the observed m_{5007} values thanks to our precised understanding of our completeness function, our PNLF fitting methodology has the potential to also constrain possible variation in the PNLF shape. This is illustrated by Fig. B.1 which shows how the distance modulus $\mu_{\rm PNLF}$ and the PNLF shape parameter c_2 of Eq. 1 are left free to vary during our PNLF fit. In this case we note a trend for over- and underestimating $\mu_{\rm PNLF}$ and c_2, respectively, for small PNe samples. The observed scatter in c_2 is quite remarkable, even for large number of PNe, but tend nonetheless to decrease with increasing numbers. As expected, also the scatter in the $\mu_{\rm PNLF}$ increases compared to the fits where c_2 was held fix, albeit only by 15%. As in the case of our single-parameter simulations, the level of completeness plays an important role in driving the accuracy in the $\mu_{\rm PNLF}$ and c_2 parameters estimation. Figs. B.2 and B.3 parallel to top and lower panel of Fig. 1 and show how deeper observations, reaching further down from the apparent magnitude of the PNLF cutoff, would lead to more accurate $\mu_{\rm PNLF}$ and c_2 measurements.

Even though in some instances such as FCC193, where we detect over 150 PNe, we could already arrive at essentially unbiased c_2 constraints within a 0.2 error, overall across the sample and after correcting for biases we cannot discern a systematic deviation from the canonical $c_2 = 0.307$ value. Finally, we note that aside from a small bias at low PNe number $\mu_{\rm PNLF}$ would also be well recovered while letting c_2 free to vary, albeit with a somewhat larger uncertainty, which demonstrates the robustness of our results when c_2 is held fix.

Appendix C: PNe maps and luminosity functions

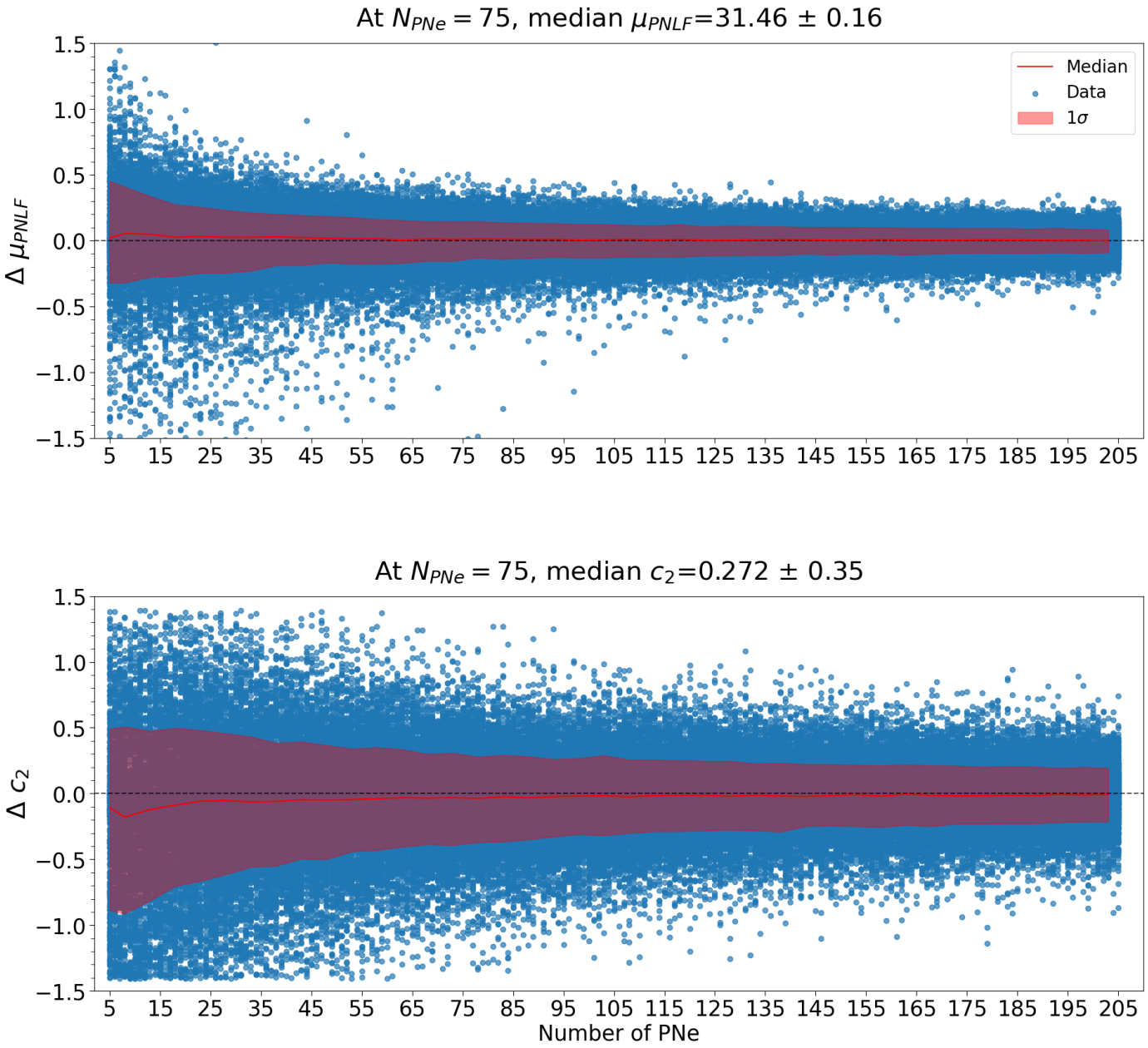

Fig. B.1: Same as Fig 2, but now while optimising both the distance modulus $\mu_{\rm PNLF}$ and the PNLF shape parameter c_2. The parent distribution assumes a distance modulus $\mu_{\rm PNLF\,in}$ = 31.45 and a standard c_2=0.307 value. As in Fig 2, the simulations also account for the whole range of completeness profiles observed across our sample.

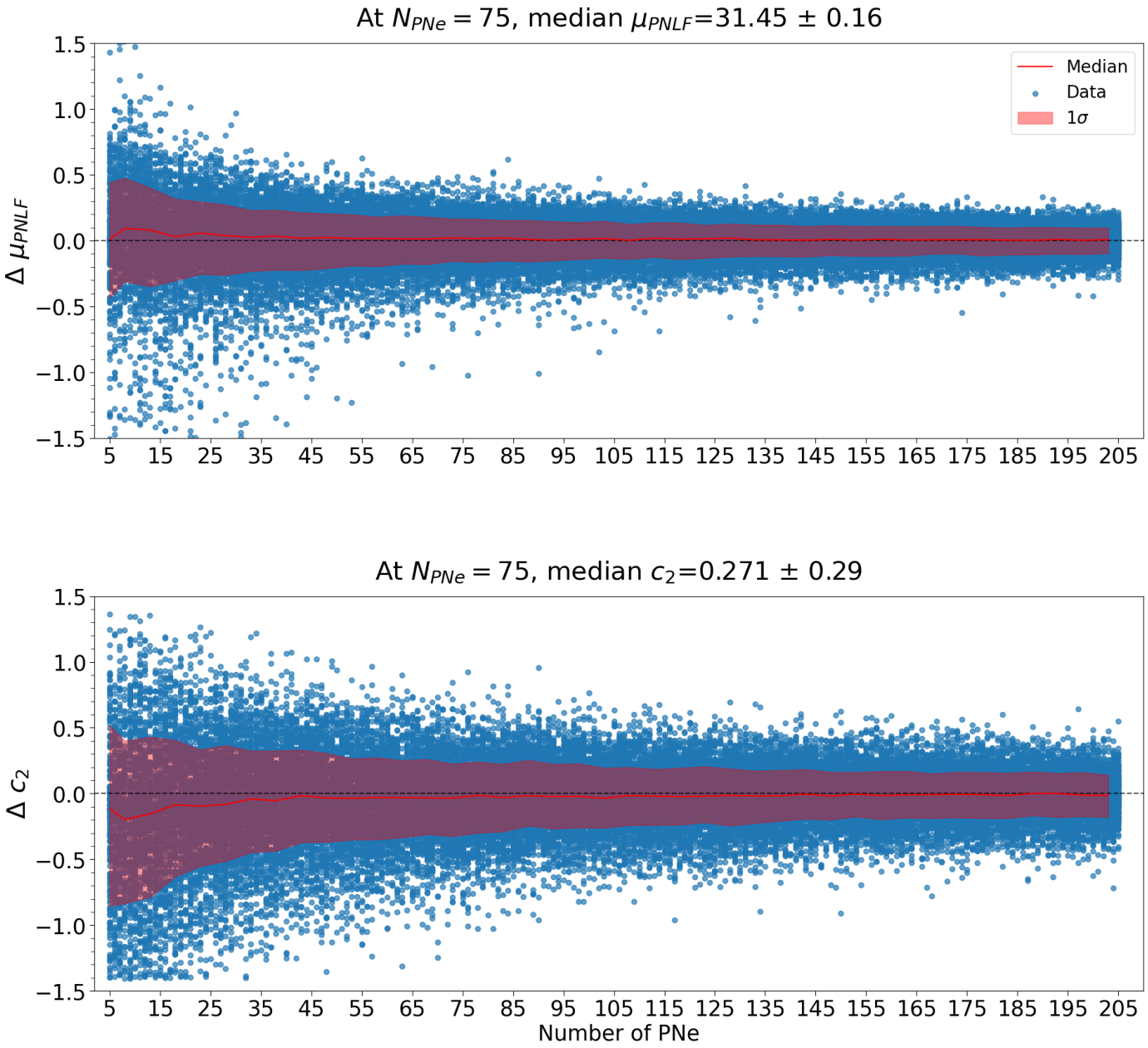

Fig. B.2: Same as Fig. B.1, but now adopting the completeness function observed in FCC 193, which extends 2.5 magnitudes from the apparent magnitude of the PNLF cutoff.

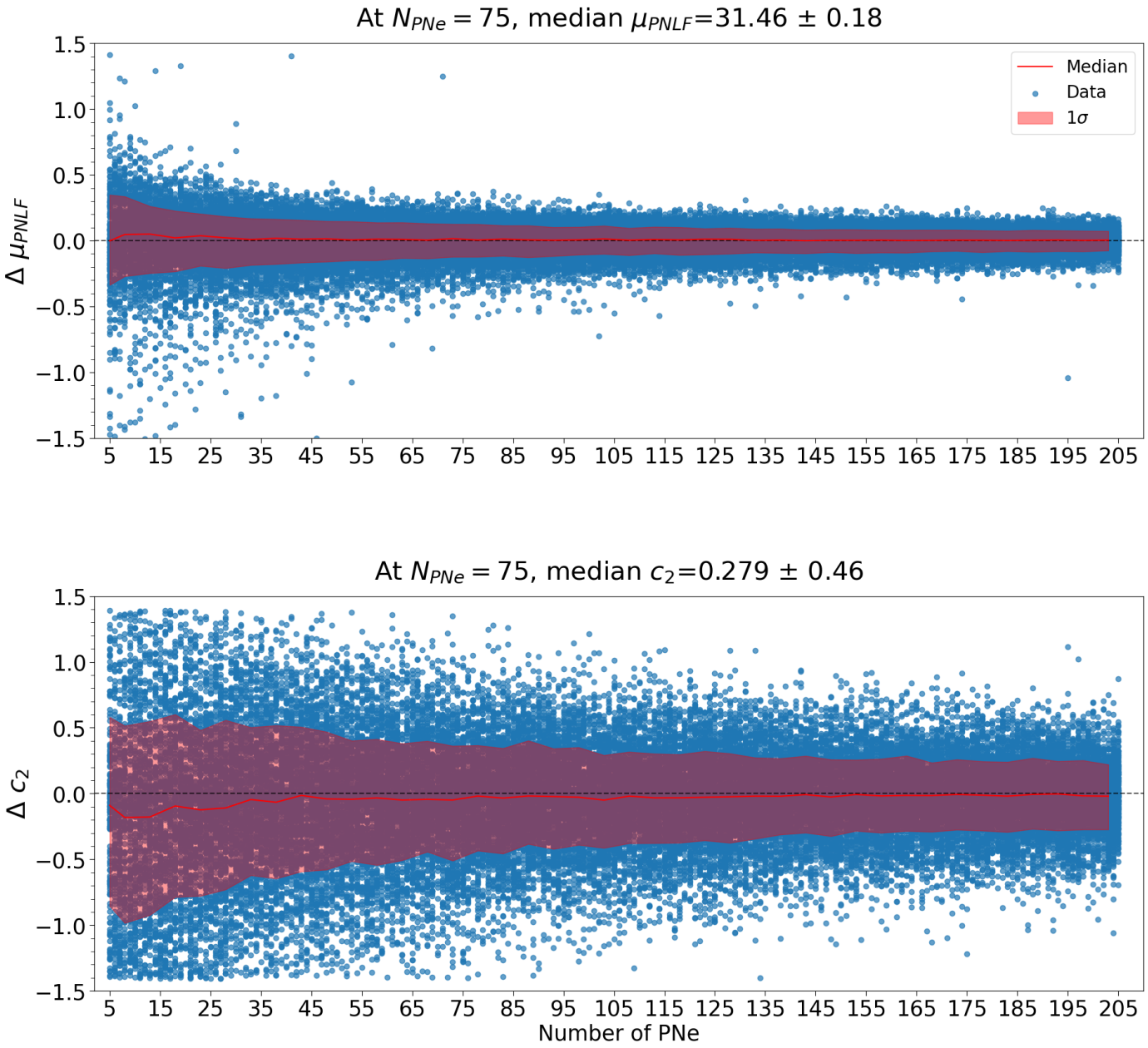

Fig. B.3: Same as Fig. B.1, but now adopting the completeness function observed in FCC 147, which extends only 1.5 magnitudes from the apparent magnitude of the PNLF cutoff.

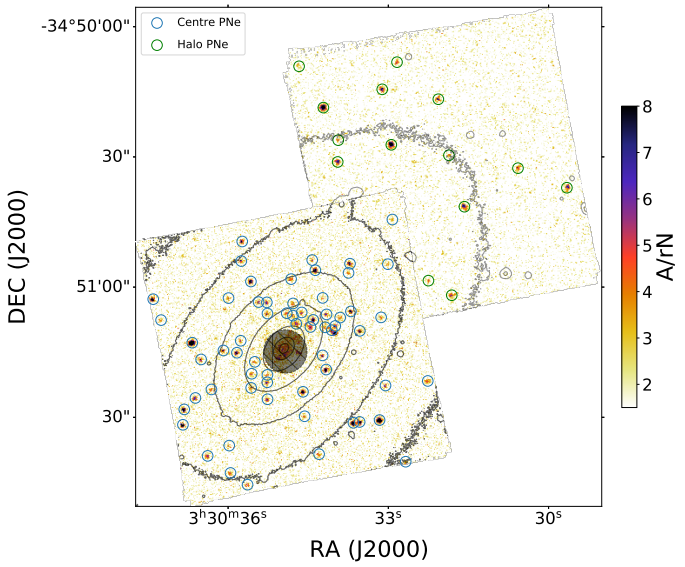

FCC083

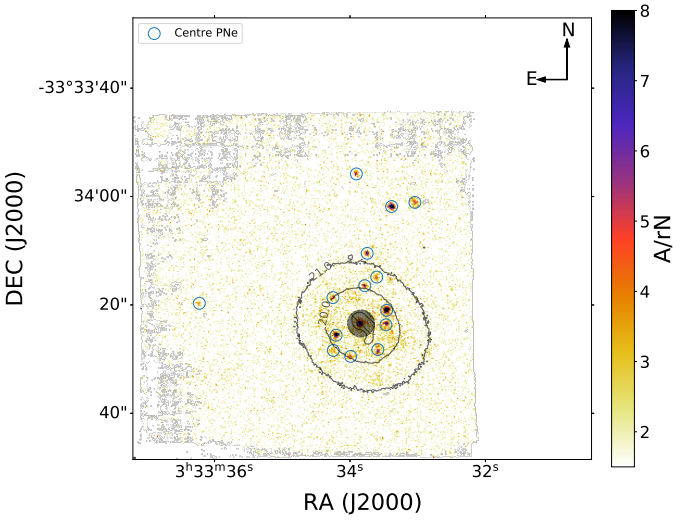

FCC119

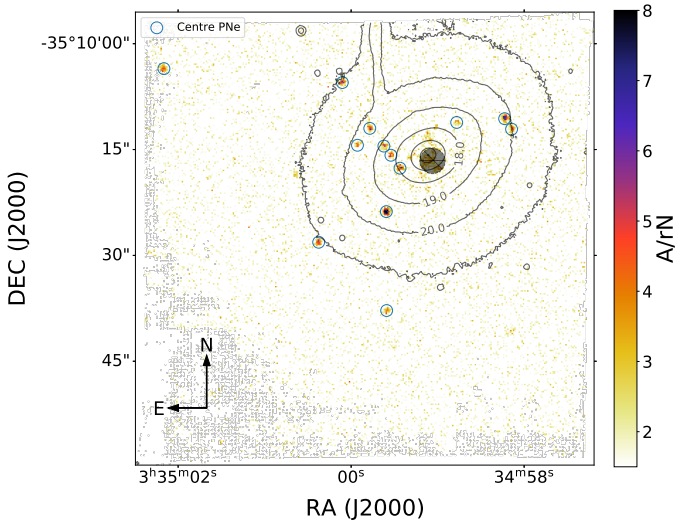

FCC143

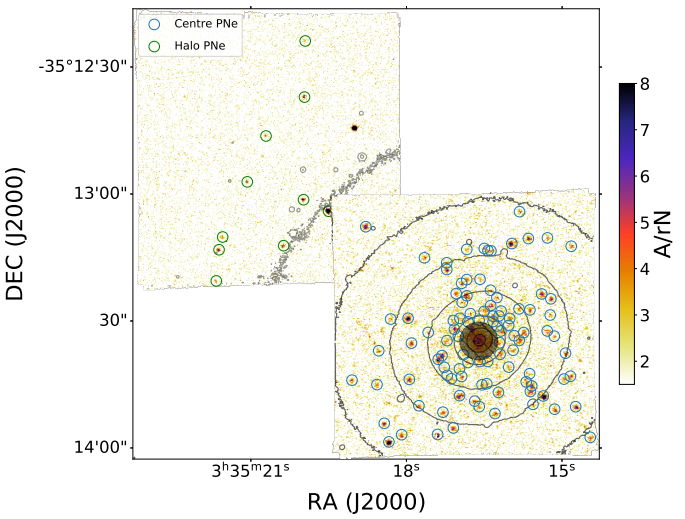

FCC147

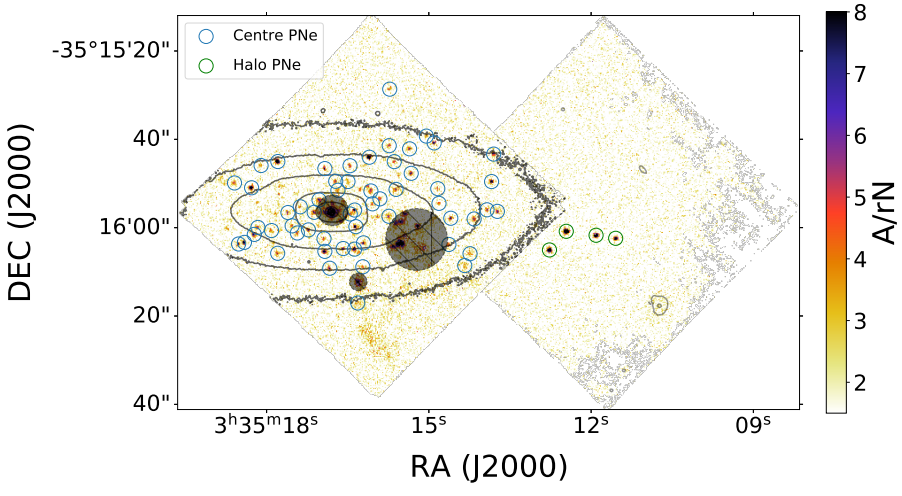

FCC148

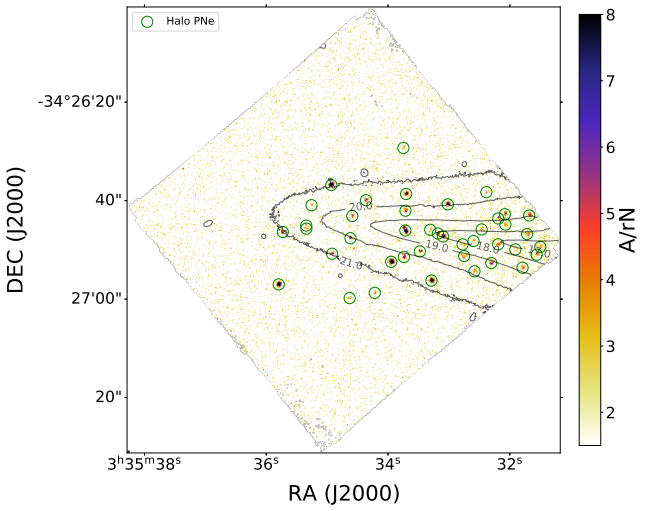

FCC153 - Halo

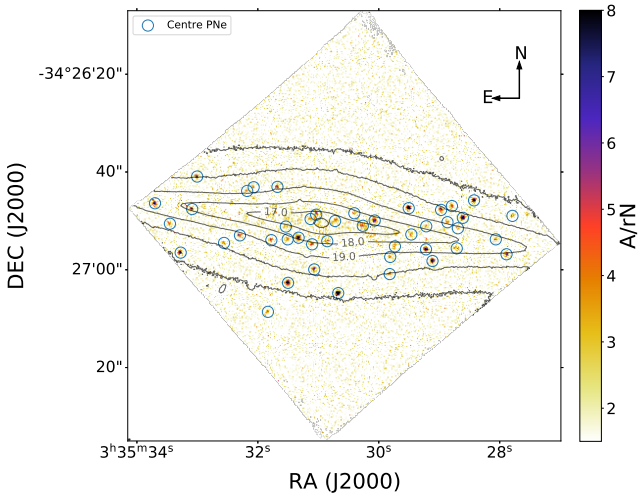

FCC153 - centre

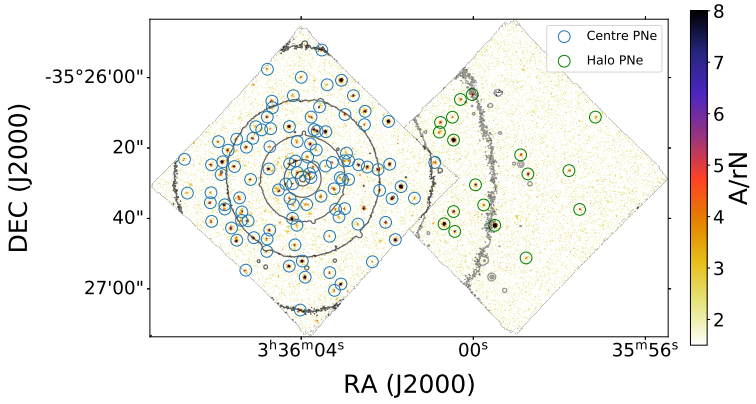

FCC161

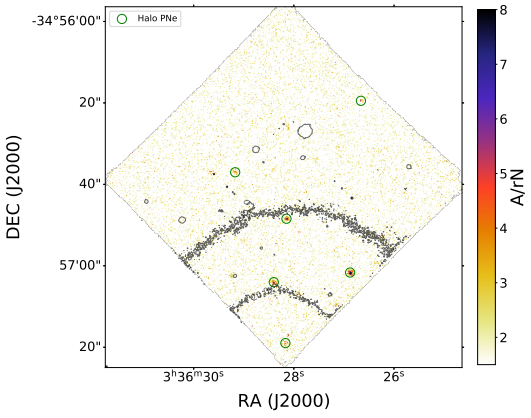

FCC167 - Halo

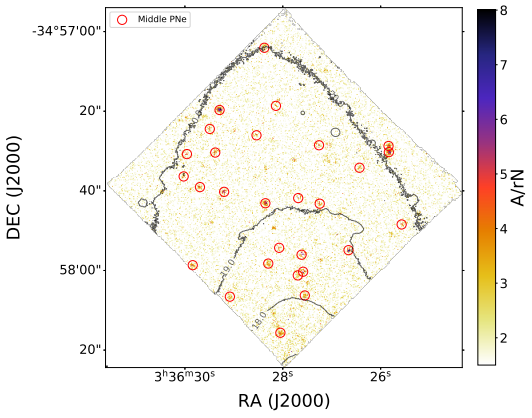

FCC167- Disk

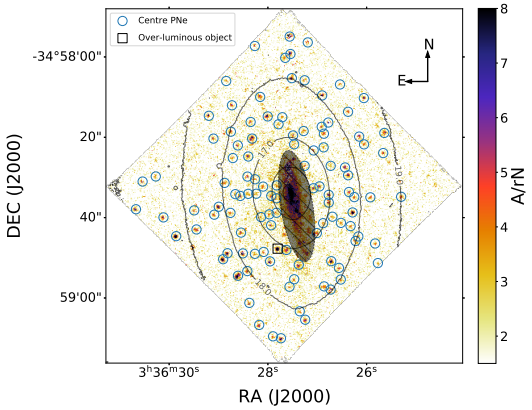

FCC167 - Centre

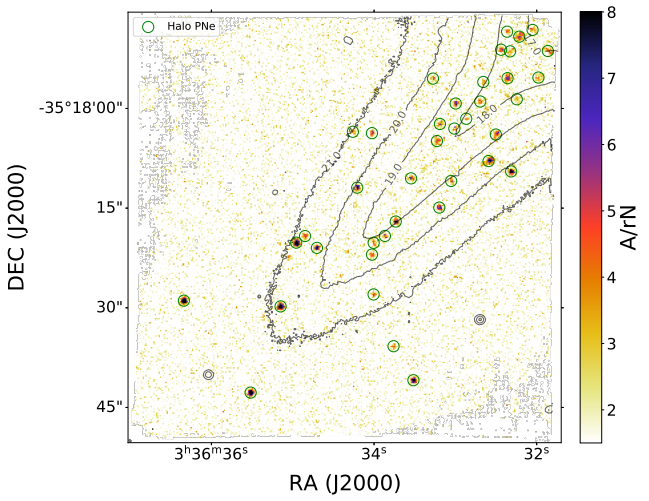

FCC170 - Halo

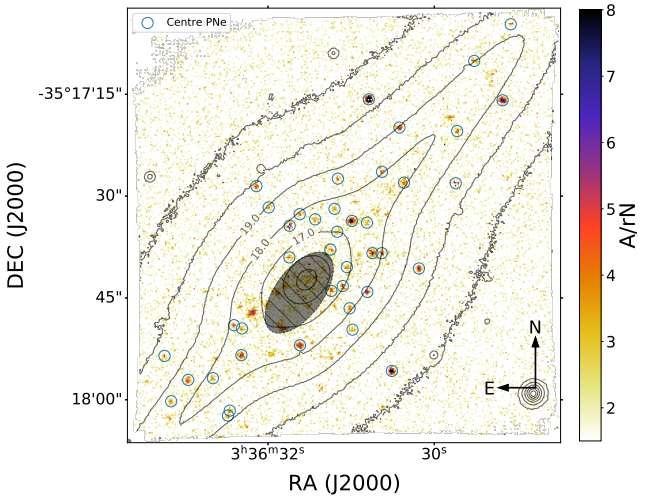

FCC170 - Centre

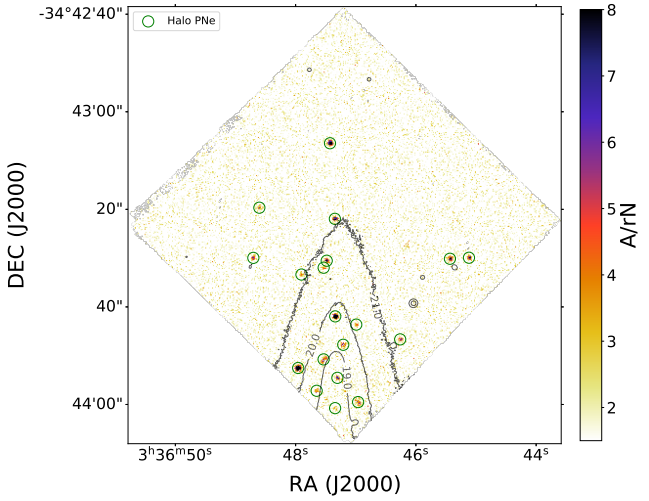

FCC177 - Halo

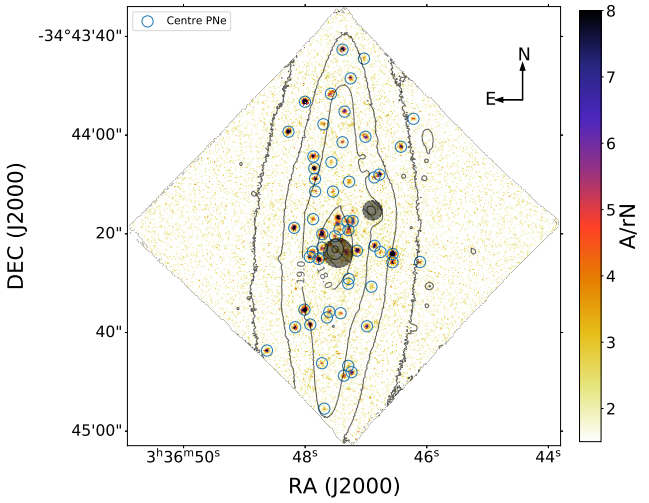

FCC177 - Centre

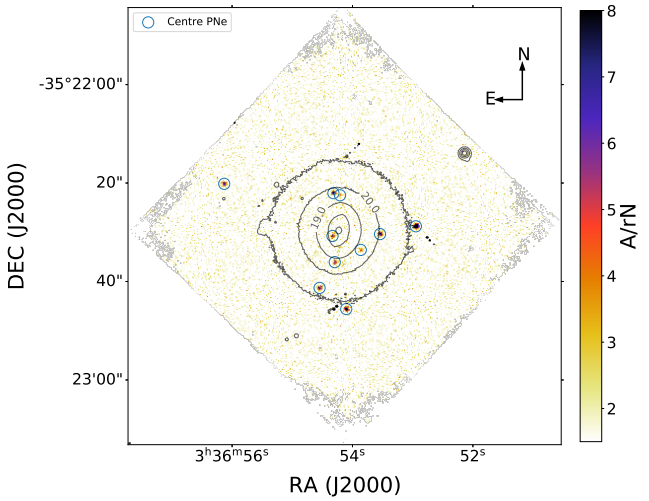

FCC182

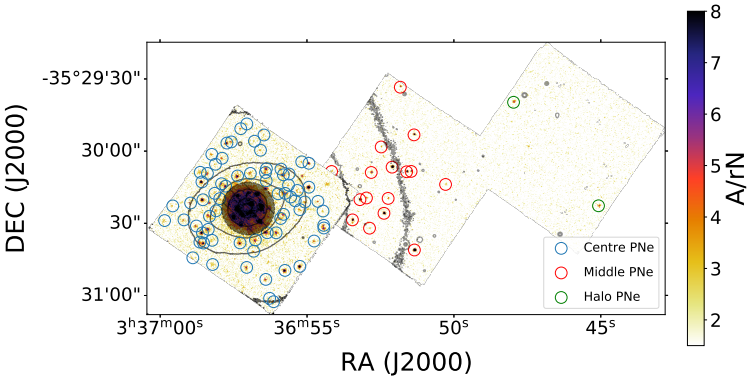

FCC184

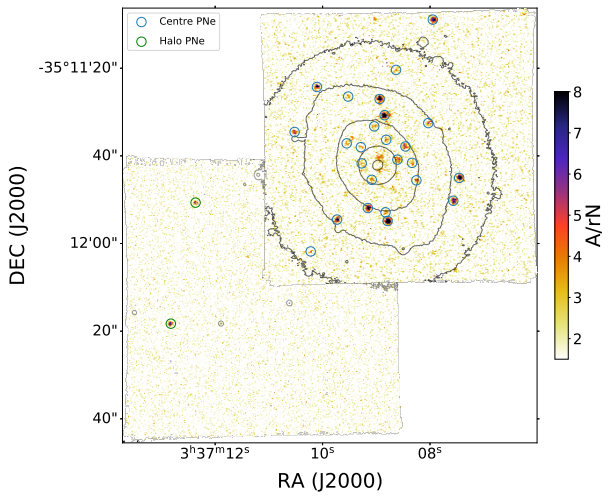

FCC190

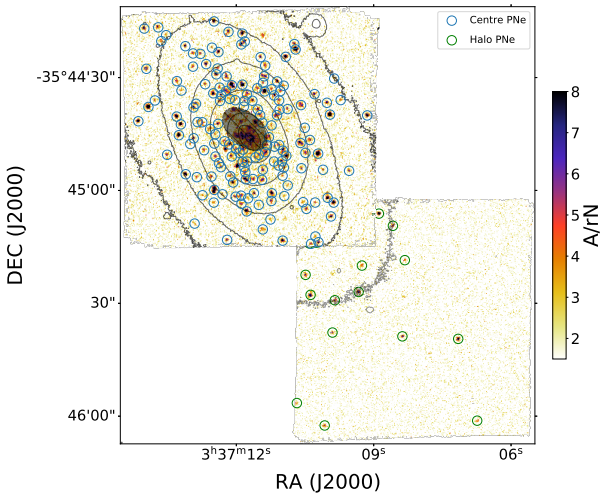

FCC193

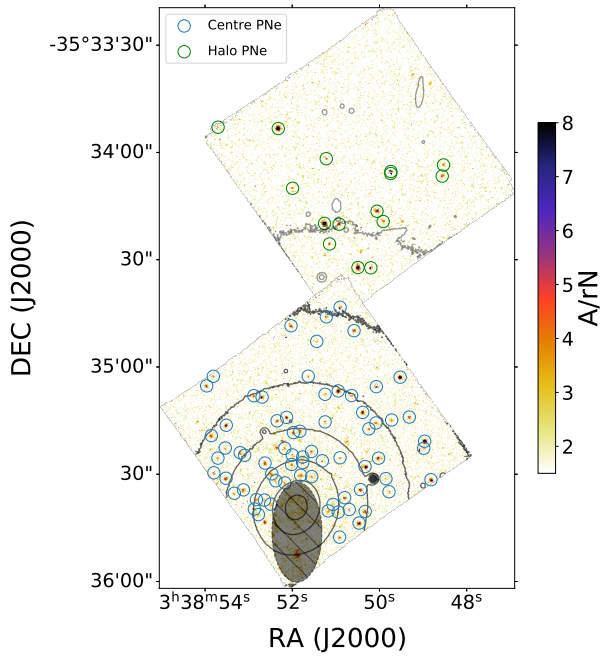

FCC219

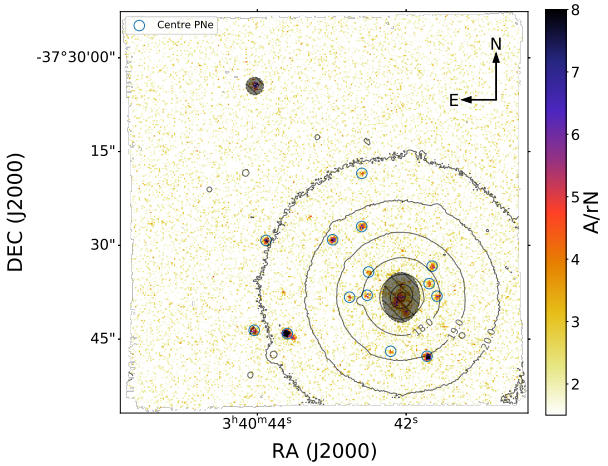

FCC249

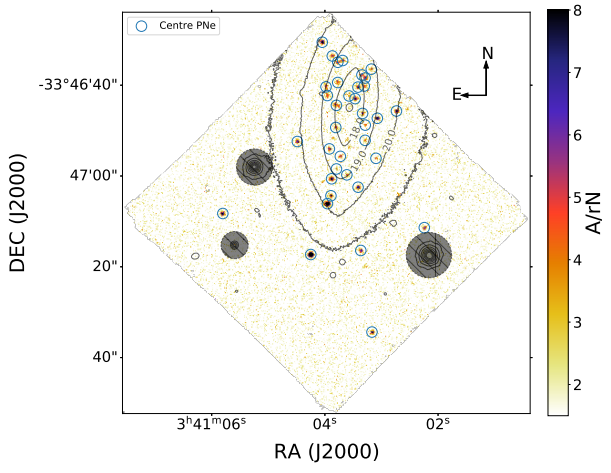

FCC255

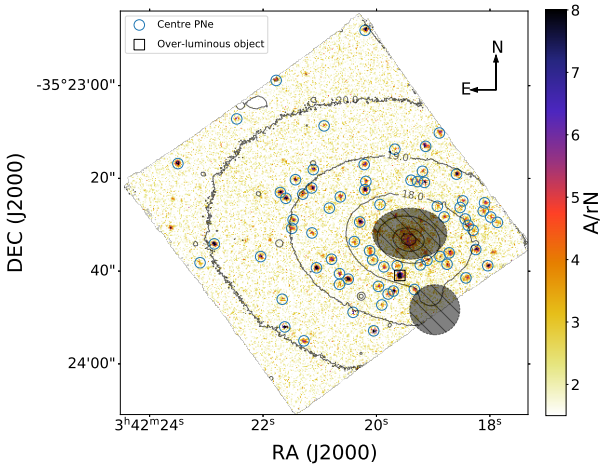

FCC276

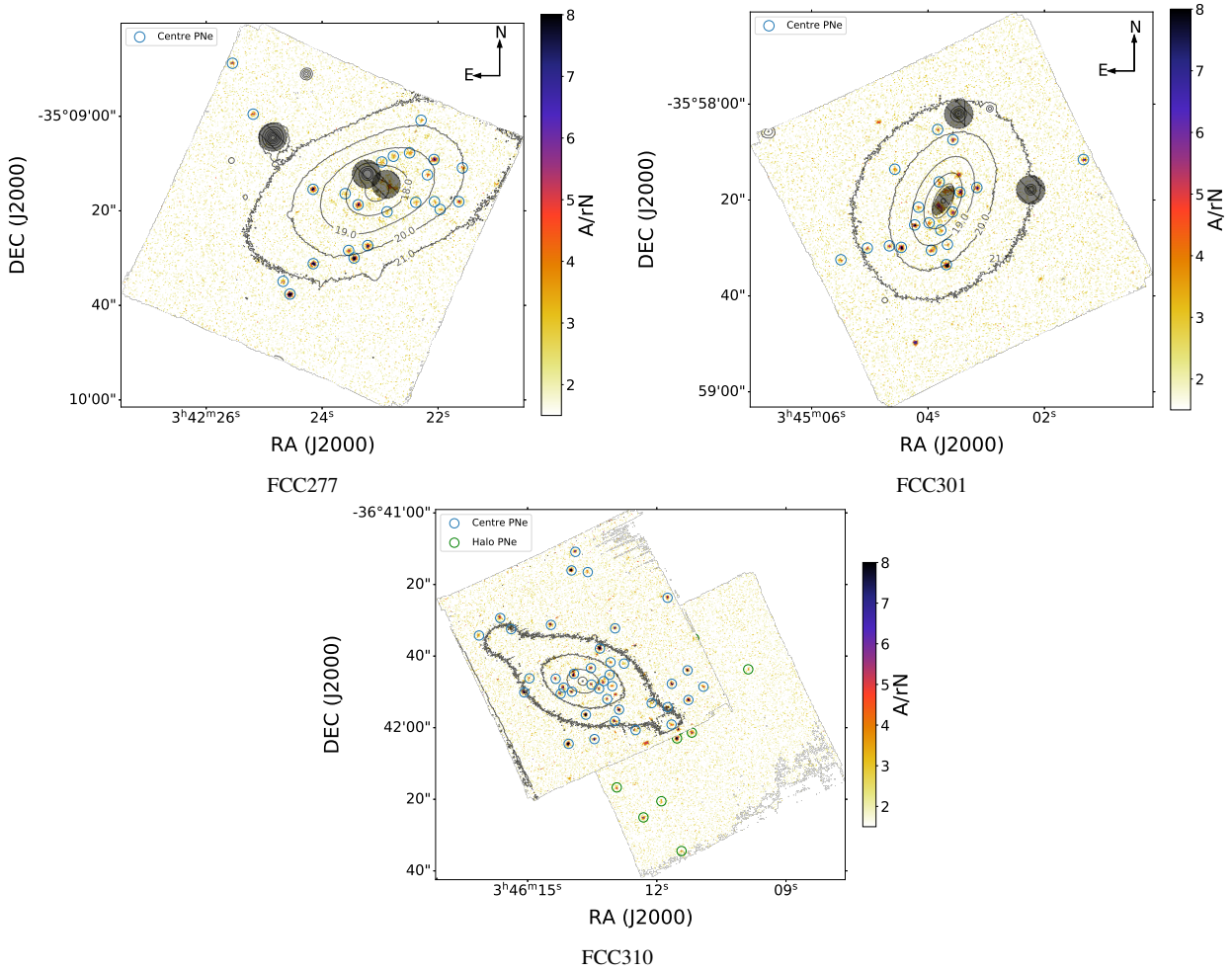

Fig. C.1: Maps for the A/rN ratio between the [O III] 5007 Å line amplitude and residual-noise level derived from our spaxel-by-spaxel spectral fit to the MUSE spectra. Both central and halo pointing are shown, with detected [O III] sources identified by coloured circles: Blue for central PNe, red for Disk (or Middle) PNe and green for Halo PNe. Isophotes are spaced at one mag arcsec^{-1} intervals. The grey dashed regions indicates the area excluded from our PNe analysis.

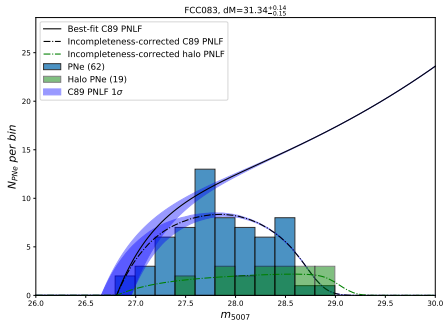

FCC083

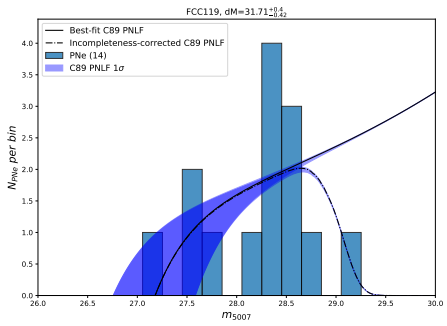

FCC119

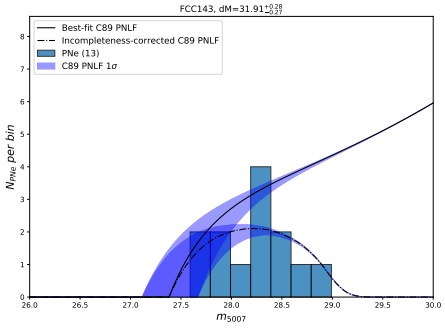

FCC143

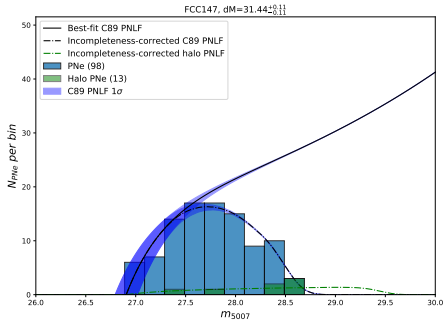

FCC147

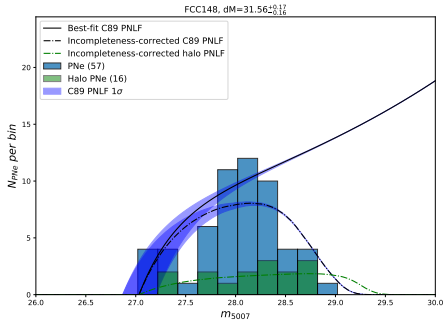

FCC148

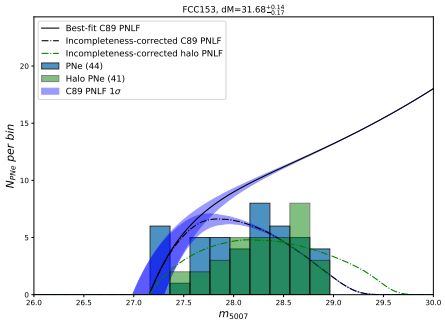

FCC153

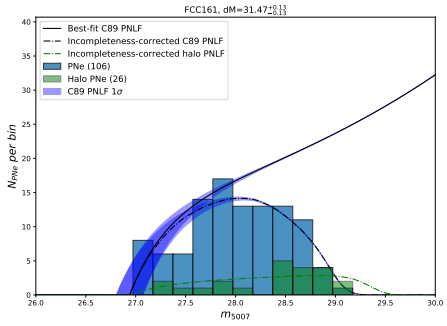

FCC161

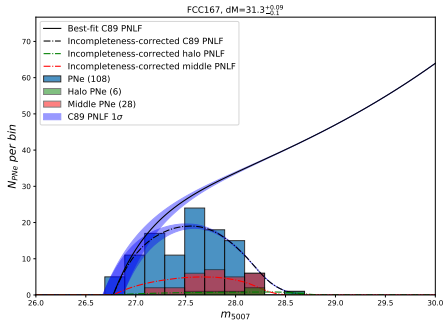

FCC167

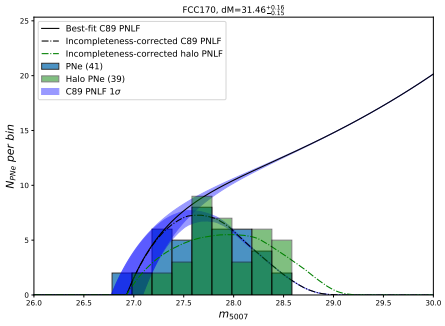

FCC170

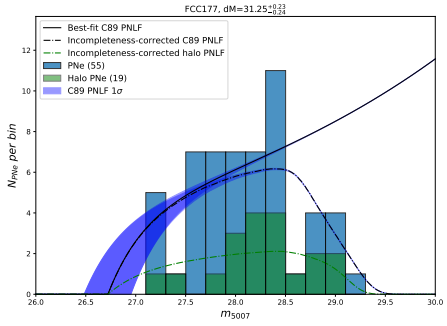

FCC177

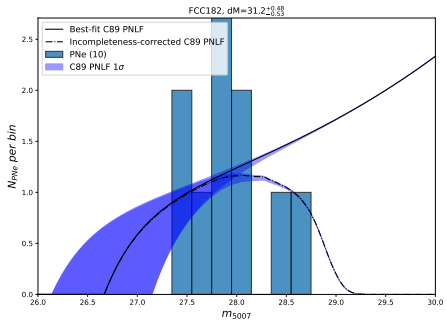

FCC182

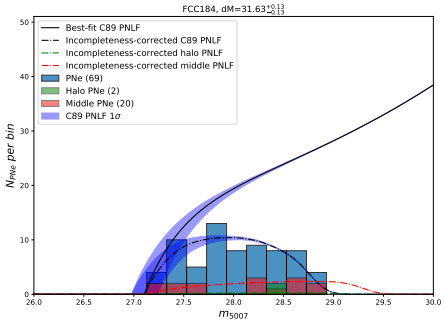

FCC184

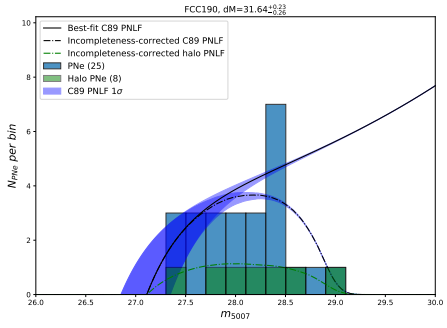

FCC190

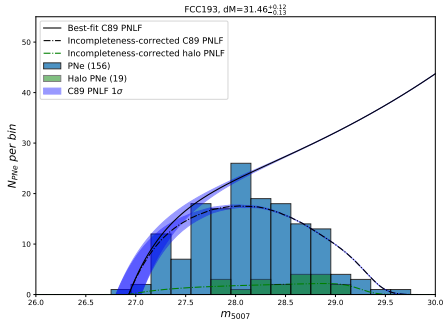

FCC193

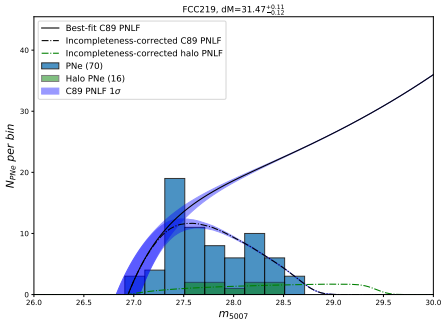

FCC219

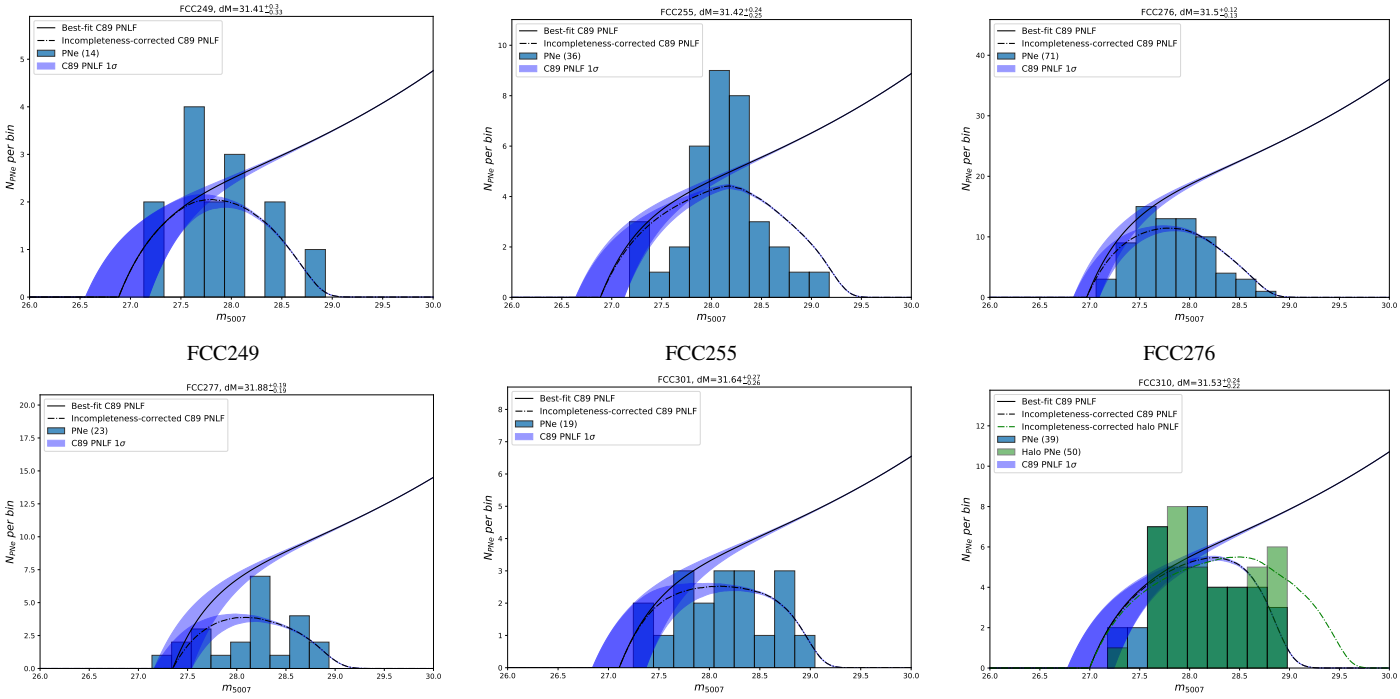

FCC249 FCC255 FCC276

FCC277 FCC301 FCC310

Fig. C.2: Observed PNLF for the PNe sources found in all the ETGs listed in 1. The entire central PNLF is fitted to derive the best distance modulus while accounting for the incompleteness of our observations. The corresponding best-fit model is shown by the dot-dashed blue line, with corresponding confidence intervals, whereas the original model PNLF - (from Ciardullo et al. 1989a) is shown by the filled blue line. Blue bars show central PNe, red bars indicate disk (or middle) PNe, and green bars show halo PNe. The green dot-dashed lines show the PNLF model at the best-fit distance modulus, corrected for incompleteness according to the depth of the halo pointing and re-scale to match its integral to the observed number of PNe in this pointing.